1458

Physics Institute, Neuchâtel University

New low background techniques for neutrino experiments at low energy. First results.

Thesis presented at the Faculty of Sciences
to obtain the Title of Doctor of Science

REDUCED FORM

Jacques Farine

December 17, 1996

IMPRIMATUR POUR LA THÈSE

Nouvelles techniques bas-bruit pour expériences neutrino à basse énergie. Premiers résultats.

de M. Jacques Farine

UNIVERSITÉ DE NEUCHÂTEL

FACULTÉ DES SCIENCES

La Faculté des sciences de l'Université de Neuchâtel sur le rapport des membres du jury,

Messieurs J.-L. Vuilleumier (directeur de thèse), J.-P. Derendinger, J. Busto, G. Gervasio et P. Hubert (Bordeaux)

autorise l'impression de la présente thèse.

Neuchâtel, le 17 décembre 1996

Le doyen:

R. Dändliker

R. Dändliker

Liste des publications

- Search for ββ decay in ^{136}Xe : new results from the Gotthard experiment.
  Physics Letters B 434 (1998) 407-414

- The MUNU experiment, general description.
  Nuclear Instruments and Methods in Physics Research A 396 (1997) 115-129

Le texte complet de la thèse est déposé à la bibliothèque de l'Université de Neuchâtel.

ELSEVIER

27 August 1998

PHYSICS LETTERS B

Physics Letters B 434 (1998) 407–414

Search for $\beta\beta$ decay in ^{136}Xe: new results from the Gotthard experiment

R. Luescher [a], J. Farine [a], F. Boehm [b], J. Busto [a], K. Gabathuler [c], G. Gervasio [a], H.E. Henrikson [b], V. Jörgens [a], K. Lou [b], A. Paić [a], D. Schenker [a], A. Tadsen [a], M. Treichel [a], J.-L. Vuilleumier [a], J.-M. Vuilleumier [a], H. Wong [b]

[a] *Institut de Physique, A.-L. Breguet 1, CH-2000 Neuchâtel, Switzerland*
[b] *Norman Bridge Laboratory of Physics, Californio Institute of Technology, Pasadena, CA 91125, USA*
[c] *Paul Scherrer Institut, CH-5232 Villigen-PSI, Switzerland*

Received 1 July 1998
Editor: K. Winter

Abstract

The Gotthard Xe experiment has taken an additional 6013 hours of data with an upgraded readout system. Lower limits for the half-life of the double beta decay in ^{136}Xe are $T^{0\nu}_{1/2} > 4.4 \times 10^{23}$ yr (including 6830 hours taken in an earlier phase), $T^{0\nu\chi^0}_{1/2} > 0.72 \times 10^{22}$ yr and $T^{2\nu}_{1/2} > 3.6 \times 10^{20}$ yr at 90% confidence level. Alpha spectroscopy, as well as $\beta\alpha$ and $\alpha\alpha$ coincidence techniques lead to a determination of the activity of the gas of 10^{-12} g/g effective of ^{232}Th and ^{238}U. Evaluations of background strongly suggest that an appreciable fraction of the $\beta\beta$-candidates comes from the allowed 2ν decay.

1. Introduction

The study of nuclear double beta decay allows the test of lepton number conservation and, in particular, the search for the existence of neutrino masses of the Majorana type [1]. The process can also probe the coupling of the neutrino to the hypothetical light neutral bosons, generically named Majorons (χ^0) [2]. The Caltech-Neuchâtel-PSI collaboration has built a time projection chamber filled with Xe gas enriched to 62.5% in ^{136}Xe to investigate the double beta decay of ^{136}Xe. The fiducial volume of 180 l contains 24.2 moles (3.3 kg) of ^{136}Xe at a pressure of 5 atm. Double beta decay candidate events are selected from their topology: single continuous tracks with increased ionization at both ends ('blobs'), due to the increase in dE/dx of the stopping electrons. The experiment was performed in the Gotthard underground laboratory. The basic design and construction of the detector is described in Ref. [3]. Experimental detail and results from a first data taking period of 6830 h are presented in Ref. [4]. Limits were reported for all decay modes.

The chamber was subsequently upgraded, to reduce the background from internal radioactivities, which was limiting the sensitivity. The read-out planes of the TPC, namely the grid, the anode and the x–y planes have been identified as the major sources of internal activities, as most observed single electron tracks in the fiducial volume were coming from their direction [5]. It was thus decided to rebuild all of these planes, using a design as simple

0370-2693/98/$ - see front matter
PII: S0370-2693(98)00906-X

and as light as possible, to reduce the amount of material, and selecting radiochemically clean components. The selection was performed with our low background Ge detector, installed in a copper and lead shielding, which allows sensitivities of a few 10^{-10} g/g to ^{232}Th and ^{238}U impurities. All selected material had contaminations lower than the detecting threshold.

A new data set of 6013 h has been taken with the upgraded setup. This letter, after a brief description of the new readout planes, presents an analysis in terms of $\beta\beta$ decay of the current and previous data, as well as a background study of the new data.

2. The new read-out planes

The new anode and grid planes (Fig. 1) are mounted on both sides of one single ring, of 70 cm inner diameter, matching the active diameter of the chamber. It is made from copper and acrylic. The anode plane contains the anode wires (gold plated tungsten, 20 μm Ø), with a spacing of 4.95 mm, alternating with potential wires (plain tungsten, 1(μm Ø) for electrical separation. To avoid sold (because of radiopurity), the wires are crimped to tl frame. All anode wires are electrically connecte together.

The grid wires (also plain tungsten, 100 μm (are mounted in a similar way, perpendicular to tl anode wires. The distance between the grid ar anode planes is 8.5 mm.

The x–y plane is a 125 μm thick PET fc covered on both sides with a 35 μm copper filr The strips, x on one side of the foil and y on tl opposite side, are made by etching. The strips a diagonal with respect to the anode and grid wires. T have a uniform lattice the spacing between strips 3.5 mm (which is that between the anode wir divided by $\sqrt{2}$). The pattern is such that the scree ing between x and y strips is minimal. The foil stretched and glued on a frame, also made fro acrylic and copper. This frame is screwed, alor with the frame for the anode and grid planes on tl lid of the copper vessel. The x–y plane is located mm behind the anode plane.

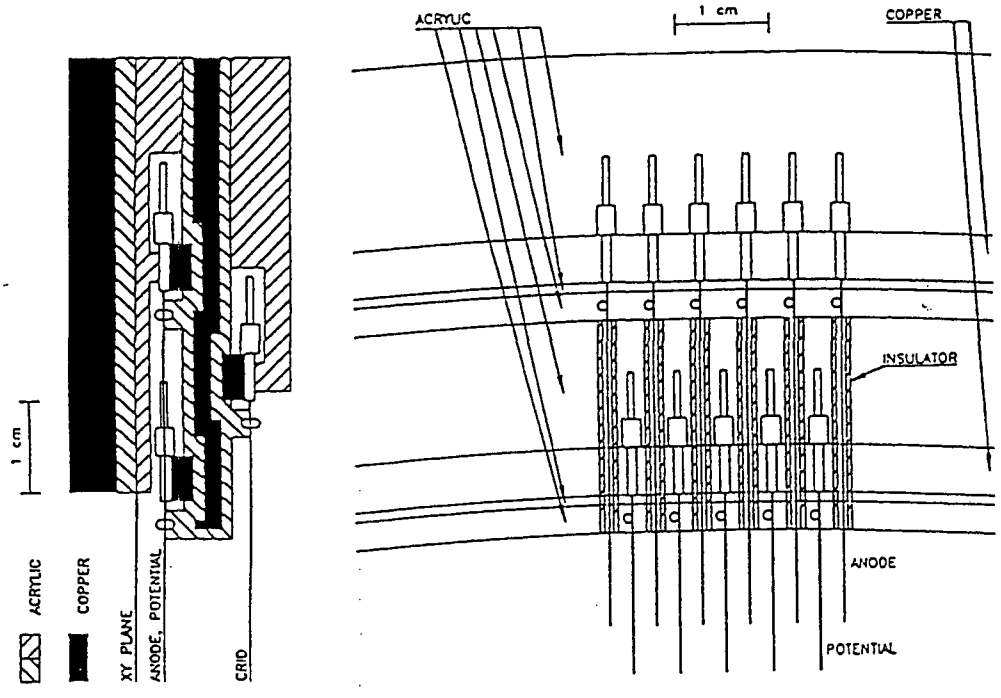

Fig. 1. Top and side view of the readout planes. The wires are fixed to the frames with crimped copper needles. Copper pins are positionir the wires at a precision of 10 μm.

This design is similar to that used for the the read-out planes of a larger TPC, MUNU, built to study $\bar{\nu}_e e^-$ scattering near a nuclear reactor. More details can be found in a paper on that detector [6].

The read-out electronics was not changed. The architecture and functionality are described in [3]. The anode signal, after integration, provides the energy information. The signals from the x–y strips are first fed into current-voltage preamplifiers, and then into two level discriminators. The first level is set below that of minimum ionizing particles, the second one is 10 times higher. It fires where the ionization density is high, for example at the end of electron tracks and for α particles. The anode is sampled at 8 MHz, the x and y strips at 2 MHz. The spatial information along the z axis is reconstructed from the time evolution of the signals. The x–z and y–z projection of each event are recorded, as well as the anode signal.

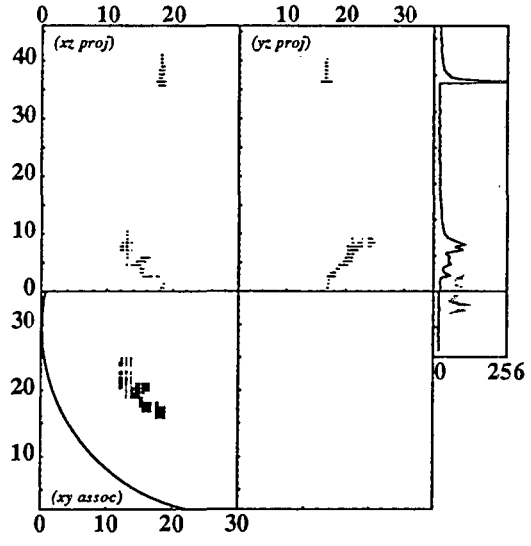

Fig. 3. $\beta\alpha$ coincidence: a single electron track is followed by an alpha emission (with a characteristic drop-like track and fast anode pulse) 28 μs later, at the same x and y position. Scales are in cm. The beta event is emitted in the direction of increasing z, defined as 'up'.

3. Detector performance

The advantage of a TPC lays in its tracking capability, allowing event recognition and good background reduction. For instance, recorded events are shown in Figs. 2 and 3: the x–z and y–z projections, as well as the corresponding anode signal are displayed in the three upper frames; below, the deduced x–y projection is drawn. The small and large 'pixels' indicate the low and high local ionization density, respectively, as given by the two level read-out discrimination. The vertical z axis calibration relies on the time sampling of 2 MHz for the strips signal: with a measured drift velocity of 1.29 cm/μs, it corresponds to an effective vertical bin size of 6.5 mm and points from the read-out plane to the cathode. The $z = 0$ time is defined by the leading edge of the anode signal.

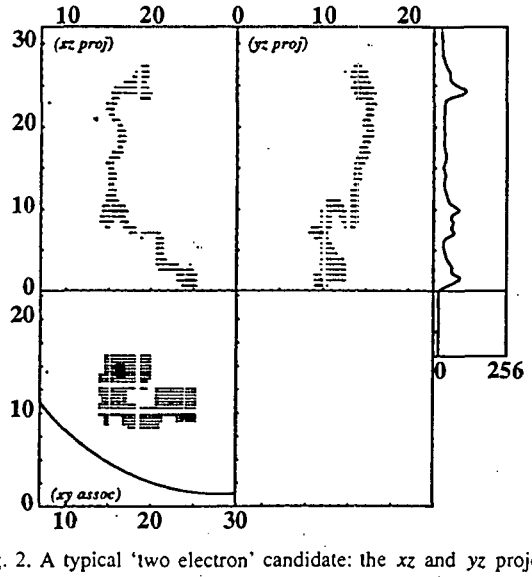

Fig. 2. A typical 'two electron' candidate: the xz and yz projection, as well as the extracted $x-y$ projections (in the lower frame) are drawn. Scales are in cm. The time evolution of the anode signal is displayed on the right. The $\beta\beta$-candidate exhibits 'blobs' at *both* ends of a continuous track.

Fig. 2 shows a typical 'two-electron' candidate, with blobs at both ends of the track. Fig. 3 depicts a beta decay (single electron, with one blob only) in coincidence with an alpha emission 28 μs later. The characteristic track and anode pulse of the alpha particle is due to the higher charge density. These specificities are not only useful for good event selection, they also make it possible to search for the origin of the background (see Section 5).

The energy measurement is obtained by integrating the digitized anode signal over the drift time. The

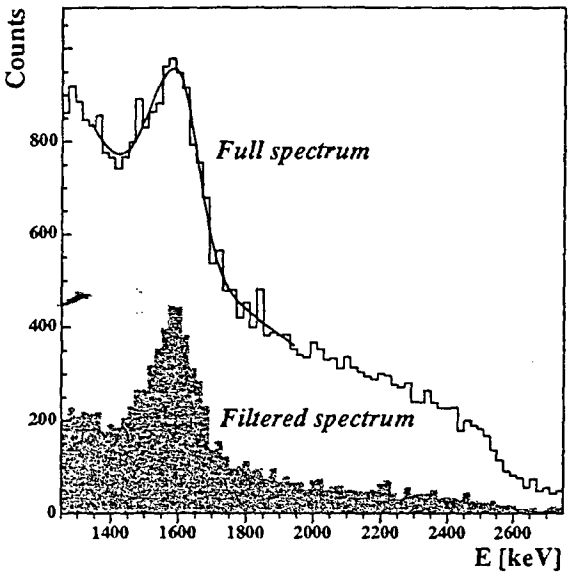

Fig. 4. Energy spectrum of a ^{232}Th source. The peak is due to the double-escape of the 2614-keV γ-rays in ^{208}Tl. The full spectrum is shown, as well as the spectrum obtained after filtering the events with our track-reconstruction program (selecting 'two-electron' events).

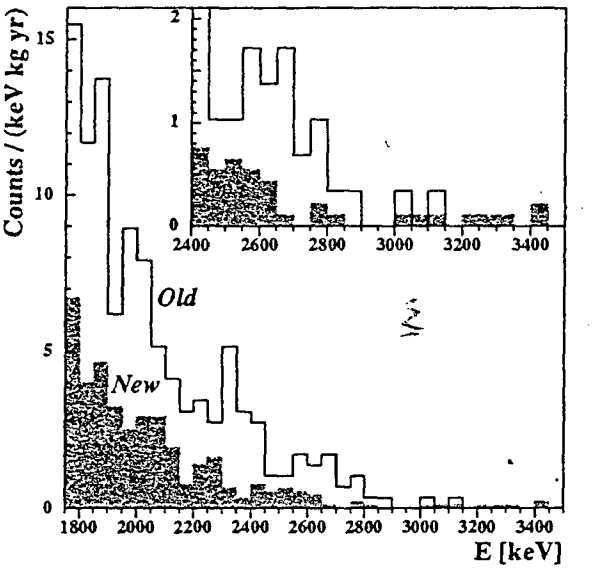

Fig. 5. Single electron spectra: comparison of count rates between data from the previous and from the new setup. A reduction of 2.8 has been achieved, slightly increasing with the energy.

energy calibration is done by measuring various γ-source spectra. It is linear in our range of interest (1–3 MeV). An accuracy to better than 2% is achieved over the whole acquisition time. Adopting similar procedures as in our previous work [4], a gain map has been established to compensate for variations across the x–y plane. The map was found to be stable within 1% over the whole duration of the experiment.

After the map correction, an energy resolution of 8% (FWHM) at 1592 keV is measured on the double escape peak from the 2614 keV γ-line in ^{208}Tl (Fig. 4). As the energy resolution is observed to scale with the square root of the energy (by measuring the width of γ-peaks from ^{22}Na, ^{137}Cs, ...), we conclude that it is 6.6% at the 0ν transition energy (2481 keV).

4. Data analysis and results

Single electron tracks with 'blobs' from δ-electron at their beginning or more complex winding shapes may mimic two electron events and represent the most troublesome background to reject. A good estimation of the achieved background reduction is therefore obtained by looking at the single electron count rate. A single electron spectrum has been obtained by visually scanning 308 h of data. A reduction factor of 2.8 has been evaluated for events in the energy range of interest comparing with our earlier work. The reduction is slightly greater at higher energies (Fig. 5 and Table 1).

The direction of emission has also been analyzed. According to the topology of their tracks, the single electrons have been classified as 'up' (possibly originated on the anode plane, as shown in Fig. 3), 'down' (coming from the cathode) or from undetermined origin: gas (tracks winding on itself), field

Table 1
Single electron count rate and direction-ratio comparisons between the previous and the current data

Energy range	Count rate (h^{-1})		'Up/down' ratio	
	old read-out	new read-out	old read-out	new read-out
> 1600 keV	4.88	1.72	4.8 ± 0.7	3.3 ± 0.4
1600–2200 keV	4.04	1.46		
> 2200 keV	0.84	0.26		

shaping rings, walls (originating from the sides of the active volume). Comparing the previous and the new data, we observe an 'up/down' ratio reduction. This can be interpreted as being the consequence of a cleaner read-out plane, since there are relatively fewer events coming from that direction.

The event identification procedure is described in details in Ref. [7]. 'Alpha-like' tracks and saturated signals are rejected by on-line vetoes. The remaining events (about 40,000 per week above 500 keV) are recorded for off-line analysis. A track-reconstruction program identifies and rejects automatically most of cosmic (~ 100%), single and multiple Compton electrons (~ 70%). The events which survive that cut have to be scanned visually. The parameters of the vetoes in all three steps have to be slightly adjusted for small variations in the detector response through time; the parameterization is based mainly on statistics, such as the average number of pixels and blobs as a function of the energy signal.

The acceptance of each cut has been evaluated in all sub-periods in the way described in Refs. [4,7]. In addition, a new acceptance calculation procedure has been implemented: Monte Carlo events have been randomly mixed to real data and then went through the same analysis procedure. In this way, we evaluate a step-by-step scanning efficiency throughout the whole real data analysis. The two evaluation procedures are in good agreement and yield a mean scanning acceptance of 68% (the rejection efficiency of single electrons is 96.5%). The major factor in the inefficiency are tracks winding on themselves which cannot be disentangled and blobs below threshold at one end of the track. Fluctuations of a few percent of these numbers are observed, depending on the scanner and on small variations in the detector response. The scanning acceptance has to be combined with a 'detector efficiency' (the probability of having a $\beta\beta$ event fully contained in the fiducial volume), which is 30% in the energy range of interest for the $0\nu\beta\beta$ decay. More details on the Monte Carlo calculations leading to that number can be found in Refs. [4,7].

The new 6013 h of data (Fig. 6) have been analyzed in terms of the $0\nu\beta\beta$ decay. We have adapted a smooth curve to the experimental points using a procedure based on Poisson statistics, as in our previous work [4]. The curve consists in an exponential background up to 2650 keV and a constant one above this energy. The cutoff at 2650 keV corresponds to the Compton edge (folded with the resolution) from the 2614 keV γ-line from ^{208}Tl, the most prominent γ-peak from natural activities in the region of interest. Good agreement is found. The new spectrum does not confirm the presence of a hole at 2500 keV, suggested in the old data with little statistical significance however. The probability of a Gaussian peak to be present above background at 2481 keV, the transition energy, was evaluated again using Poisson statistics. No evidence of a peak is found. This translates into the half-life limit given in Table 2.

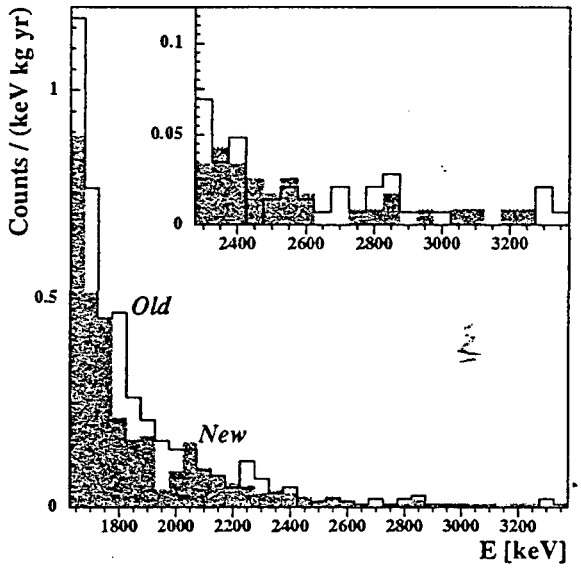

Fig. 6. Two electron spectra for the old (6830 h or 2.6 kg×yr) and for the new (6013 h or 2.3 kg×yr) data. The reduction of count rate is significantly smaller than for single electrons. This, together with background considerations, is an indication that an appreciable fraction is due to the $2\nu\beta\beta$ decay.

The best sensitivity is obtained by analyzing in the same way the entire data set: the old and the new

Table 2
Half-life limits for the $0\nu\beta\beta$ decay: comparison between the 90% C.L limits obtained from the previous, the current and the total data

	Acquisition time (h)	$T^{0\nu}_{1/2}$ 90% C.L. limit (yr)
previous data [4]	6830	$> 3.6\times10^{23}$
new data	6013	$> 1.7\times10^{23}$
total	12843	$> 4.4\times10^{23}$

data are summed up and give a spectrum corresponding to 12843 h of data (Fig. 7). Again no evidence of a peak is found. From this, a half-life limit is derived, which improves on our previous result. From that, limits on the effective Majorana mass are derived and shown in Table 3, using different nuclear matrix element calculations. These limits are the most restrictive ones after those obtained in ^{76}Ge by the Heidelberg-Moscow collaboration [13].

For the study of the Majoron $0\nu\chi^0\beta\beta$ and the allowed $2\nu\beta\beta$ decay mode, low background is more important than statistics. Therefore, only the 6013 h of new data have been considered to evaluate the corresponding limits. No background subtraction has been performed. For the $0\nu\chi^0$ decay, the integral count rate in the energy region between 2150 and 2400 keV (containing 11.8% of the decay spectrum, taking Coulomb-corrections and energy resolution into account), including possible upwards statistical fluctuations, was taken as the largest possible event rate. From this, a half-life limit (at 90% C.L.) of

$$T^{0\nu\chi^0}_{1/2} > 0.72 \times 10^{22} \text{ yr}$$

was obtained. The corresponding limit for the neutrino-Majoron coupling constant $\langle g_{\nu\chi^0} \rangle$ are shown in Table 2 for different nuclear matrix element calculations.

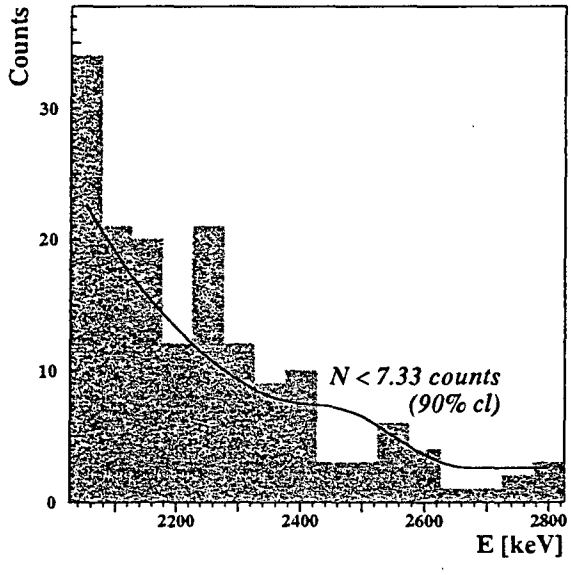

Fig. 7. Two electron energy spectrum for the summed old and new data (12843 h or 4.9 kg × yr). No evidence of a $0\nu\beta\beta$ peak is found. The 90% C.L. limit for a hypothetical 0ν peak at 2481 keV, corresponding to $T^{0\nu}_{1/2} > 4.4 \times 10^{23}$ yr, is drawn.

Table 3
Effective majorana mass of the neutrino and neutrino-Majoron coupling constant, derived from the measured 90% C.L. half-life limit of the $0\nu\beta\beta$ and the $0\nu\chi^0\beta\beta$ decay in ^{136}Xe, respectively. Different nuclear matrix element calculations are used

Nuclear matrix elem. model	m_ν	$\langle g_{\nu\chi^0} \rangle$
Caltech [8]	< 2.4–2.7 eV	$< 2.0 \times 10^{-4}$
Heidelberg [9]	< 2.2 eV	$< 1.6 \times 10^{-4}$
Tuebingen I [10]	< 1.8 eV	$< 1.3 \times 10^{-4}$
Tuebingen II [11]	< 2.0–2.5 eV	< 1.4–1.8×10^{-4}
Strasbourg-Madrid [12]	< 5.2 eV	$< 3.8 \times 10^{-4}$

A similar procedure was applied for the $2\nu\beta\beta$ decay, with an energy interval from 1750 to 2000 keV (corresponding to 1.8% of the decay spectrum). The limit is (at 90% C.L.):

$$T^{2\nu}_{1/2} > 3.6 \times 10^{20} \text{ yr.}$$

We note that the two electron count rate shows a significantly lower reduction than the single electron count rate, comparing the new and old spectra (Fig. 6). This indicates that an appreciable fraction of our $\beta\beta$ candidates may be due to the allowed $2\nu\beta\beta$ decay. A calculation based on QRPA calculations predicts $T^{2\nu}_{1/2} = 8.5 \times 10^{20}$ yr [1]. However, a longer half-life of $T^{2\nu}_{1/2} = 1.7$–2.0×10^{21} yr is predicted by a recent shell model calculation [12].

5. Background investigations

To confirm that we see double beta decay, we must understand better our background. Electron-positron pairs produced by γ-rays can mimic two electron events in the TPC and in principle contribute to the two electron background. We note however that the highest γ peak in the natural chains is the 2614 keV ^{208}Tl line. The corresponding electron-positron pair has an energy of 1592 keV. Our analysis is restricted to the energy range above 175C keV, in which we can neglect pair production as a background source.

The other potential source of two electron background are misidentified single electron which, we believe, dominate. Considering that a single electror

as a probability of 3.5% to be misidentified as two lectron event (as the rejection efficiency is 96.5%), nd starting from the measured single electron back-round, we can calculate the contribution to the two lectron count rate. It turns out to be about half of ıe observed rate in the energy window of interest etween 1750 and 2000 keV.

We made an effort to pin down the sources of the ackground. Alpha spectroscopy is useful to identify ıe internal background sources. Alpha events pre-ːnt a fast pulse shape (generally saturating the ectronics) and a typical drop-like feature (Fig. 3). or the purpose of an alpha spectroscopy analysis, a ɔecific data set of 143 h has been taken: a 6 dB tenuator had been added to the anode output to ːevent saturation of the ADC. In addition, a soft-are post-trigger delay has been used, waiting for a ɔssible second event in the time lapse of 100 ms he track was then recorded in the same readout): is additional accurate space and time information is ːeful for a short time coincidence analysis. Also vestigations about long coincidences (up to 300 s) ıve been performed, analyzing events from succes-ve readouts. Time resolution is then given by the ımputer clock.

The alpha decays present clearly different pulse-ape and tracking features than those from β-like ents. An α-selecting software has therefore been ıplemented, reaching an efficiency of 99%. The sulting α-spectrum is shown in Fig. 8. Due to ıenching effects, the alphas have a different gain d gain-map than β-like events. There is a domi-nt peak in the spectrum, strong enough to be used r establishing an α-map. After energy correction, a ɔolution of 3.8% (FWHM) is achieved at the peak ːition (further analysis will show that it corre-onds to 5.3 MeV, the kinetic energy of the α-par-les emitted in the disintegration of ^{210}Po).

Successive events are considered as coincidence if ːir position (for alphas), or starting point (for tas) are within a circle of radius 1.4 cm (or 4 ips) in the xy-projection. The starting point of tas has to be established by eye: 61.5 h of the runs have been scanned visually for the purpose of r coincidence investigation. Two $\beta\alpha$ sequences ve been identified by applying time cuts [14]: the line of the 'short' ^{212}Bi–^{212}Po coincidence ap-ars by selecting successions of $\beta\alpha$ decays happen-

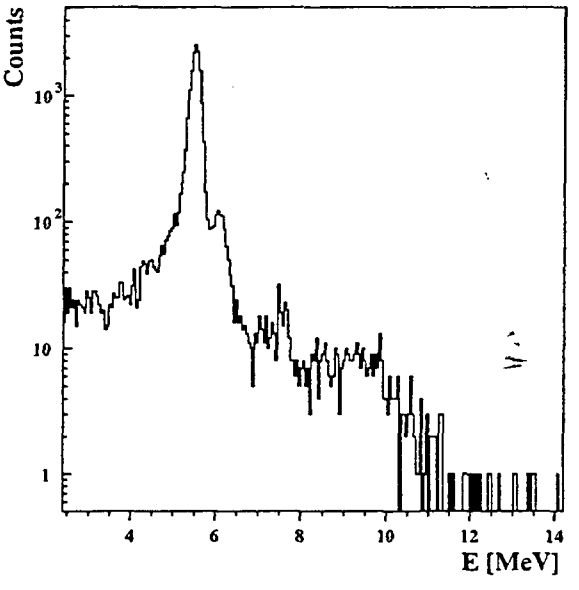

Fig. 8. Energy spectrum of α-events, taken on a specific run (143 h with no on-line vetoes). The alphas are selected by software. A specific α-map-correction has been applied. The calibration is obtained from the identification of α-lines through coincidence investigations.

ing within a time interval smaller than $\Delta t = 1.5\ \mu$s; the α-line of the 'long' ^{214}Bi–^{214}Po sequence (Fig. 3) is observable with a '$\Delta t > 1.5\ \mu$s' cut. From the direction of the beta tracks one concludes that these contaminations are concentrated on the cathode (the 'up/down' ratio is 0.3 ± 0.1).

The $\alpha\alpha$ coincidences are overwhelmed by the dominant peak-structure even when applying only specific time-windows. Additional energy windows have therefore been established around the first decay (or the second, for cross-check purpose) to enhance the second one (respectively the first one) in the α-spectrum. The ^{222}Rn–^{218}Po and ^{220}Rn–^{216}Po lines have been observed this way [14].

From the recognized lines, an α-calibration has been established: we deduce a quenching factor of ~ 6.5 for alphas in Xe at 5 bars.

Effective contaminations have been estimated (assuming secular equilibrium and normalized to the total Xe mass) from the $\alpha\alpha$ and $\beta\alpha$ coincidences rates to be at the level of 5×10^{-12} g/g for ^{232}Th and 9×10^{-12} g/g for ^{238}U. From these two chains, only the β-decay of ^{214}Bi could contribute in the $0\nu\beta\beta$ energy region. It has a $Q_\beta = 3.26$ MeV, with

a relative intensity of 19%. From the ^{214}Bi–^{214}Po–$\beta\alpha$-coincidence rate of 2.2 ± 0.3 per hour and taking into account the efficiency and the containment probability, we conclude that this contribution to our single electron spectrum is at most 10%. This background source is thus not dominant in the two electron spectrum.

The dominant peak in the α-spectrum is at the energy of the α-particles from ^{210}Po (^{238}U chain). The presence of this peak is thought to be the consequence of an exposure of the cathode to the laboratory air (where a radon level of ~ 110 Bq/m^3 has been measured) during the upgrade of the readout system. ^{222}Rn decays rapidly to ^{210}Pb, which had been collected on the surface of the cathode. We cannot tell, with our energy resolution, if the peak position corresponds to energy of the α-particle alone, which would be the case if the contamination were on the surface, or if the energy of the recoil nucleus is included, which would show that the contamination is in the gas. However, in order to verify that the contamination is on the surface, the chamber has been filled with a Ar–CH_4 mixture. The measured activity of ^{210}Po remained unchanged. Therefore, contaminations in the gas itself or originated in the gas system are unlikely. The presence of ^{210}Pb has no consequences on our $0\nu\beta\beta$ limit: the progenitors have disappeared rapidly after closing the chamber and the daughters present only betas with low Q_β.

An attempt was made to attenuate neutron activities from the surroundings by installing a new shield of 5 mm thick B_4C around the detector. The efficiency to capture neutrons has been measured using a Cf source: runs with or without the shielding show a count rate difference of 40% for β-like events in the interval from 1 to 3 MeV. Nevertheless, no change in the 'two electron' count rate has been observed in the $\beta\beta$-runs done after the installation. Neutrons are therefore not a major background source and the installation of an external moderator was not deemed necessary.

We conclude that the background in the $\beta\beta$ spectrum is dominated by misidentified single electron caused by natural γ activities. They account however for only about half of the observed two electron events. The rest maybe due to the $2\nu\beta\beta$ decay, as suggested in Section 4. In order to clearly measure the $2\nu\beta\beta$ decay, we are planning measurements at lower pressure and thus with a lower energy threshold, as well as measurements with Xe depleted in the ^{136}Xe isotope.

6. Conclusions

The upgrade of the readout planes in our ^{136}Xe TPC leads to an appreciable background reduction. Limits on $\beta\beta$-decays have been extracted from a new data-set and there are strong indications that a fraction of our $\beta\beta$-candidates are due to the allowed $2\nu\beta\beta$ mode. Special efforts and additional measurements are planned in order to identify and measure this decay.

Acknowledgements

The authors would like to thank P. Vogel for enlightening discussions, as well as the technical staff of the Institut de Physique of Neuchâtel for assistance. This work was supported by the Fonds National Suisse pour la recherche scientifique and the US Department of Energy.

References

[1] M. Moe, P. Vogel, Ann. Rev. Nucl. Part. Sci. 44 (1994) 247.
[2] P. Bamert, C.P. Burgess, R.N. Mohapatra, Nucl. Phys. B 449 (1995) 25.
[3] M.Z. Iqbal et al., Nucl. Instrum. Methods 259 (1987) 459.
[4] J.-C. Vuilleumier et al., Phys. Rev. D 48 (1993) 1009.
[5] V. Jörgens, PhD thesis, University of Neuchâtel (1993), unpublished.
[6] The MUNU Collaboration (C. Amsler et al.), Nucl. Instrum. Methods 396 (1997) 115.
[7] H.T. Wong et al., Nucl. Instrum. Methods 329 (1993) 163.
[8] J. Engel et al., Phys. Rev. C 37 (1988) 731.
[9] A. Staudt et al., Europhys. Lett. 13 (1990) 31.
[10] T. Tomoda, Rep. Prog. Phys. 54 (1991) 53.
[11] G. Pantis et al., Phys. Rev. C 53 (1996) 695.
[12] E. Caurier et al., Phys. Rev. Lett. 77 (1996) 1954.
[13] L. Baudis et al., Phys. Lett. B. 407 (1997) 219.
[14] J. Farine, Ph.D. Thesis, University of Neuchâtel (1996), unpublished.

ELSEVIER

Nuclear Instruments and Methods in Physics Research A 396 (1997) 115–129

NUCLEAR INSTRUMENTS & METHODS IN PHYSICS RESEARCH Section A

The MUNU experiment, general description

MUNU Collaboration

(Bochum–Grenoble–Neuchâtel–Padova–Zürich)

C. Amsler[a], M. Avenier[b], G. Bagieu[b], C. Barnoux[b], H.-W. Becker[c], R. Brissot[b], C. Broggini[d], J. Busto[e], J.-F. Cavaignac[b], J. Farine[e], D. Filippi[d], G. Gervasio[e], P. Giarritta[a], G. Grgić[e], B. Guerre Chaley[b], V. Joergens[e,1] D.H. Koang[b], D. Lebrun[b], R. Luescher[e], F. Mattioli[d], M. Negrello[d], F. Ould-Saada[a], A. Paić[e], O. Piovan[d], G. Puglierin[d], D. Schenker[e], A. Stutz[b], A. Tadsen[e], M. Treichel[e,2], J.-L. Vuilleumier[e,*], J.-M. Vuilleumier[e]

[a] *Physik -Institut, Winterthurerstrasse 190, CH-8057 Zürich, Switzerland*
[b] *Institut des Sciences Nucléaires, IN2P3-UJF, 53 avenue des Martyrs, F-38026 Grenoble Cedex, France*
[c] *Experimentalphysik III, Ruhr-Universität-Bochum, Universitätsstrasse 150, D-44780 Bochum, Germany*
[d] *Istituto Nazionale di Fisica Nucleare-Sezione di Padova and Università di Padova, via Marzolo 8, I-35131 Padova, Italy*
[e] *Institut de Physique, A.-L. Breguet 1, CH-2000 Neuchâtel, Switzerland*

Received 20 February 1997; received in revised form 17 March 1997

Abstract

We are building a low background detector based on a gas time projection chamber surrounded by an active anti-Compton shielding. The detector will be installed near a nuclear reactor in Bugey for the experimental study of $\bar{\nu}_e e^-$ scattering. We give here a general description of the experiment, and an estimate of the expected counting rate and background. The construction of the time projection chamber is described in details. Results of first test measurements concerning the attenuation length and the spatial as well as energy resolution in the CF_4 fill gas are reported.

PACS: 13.10.+q; 14.60.Lm; 14.60.St
Keywords: Neutrino–electron scattering; Neutrino magnetic moment; Time projection chamber

1. Introduction

The MUNU experiment has been designed to study $\bar{\nu}_e e^-$ scattering with low-energy antineutrinos from a nuclear reactor. This process, as well as $\nu_e e^-$ scattering, is fundamental, and a precise investigation may provide information on basic features of the weak interaction, and on neutrino properties.

Both charged (CC) and neutral weak currents (NC) are involved. They are expected to interfere if the NC and CC final state neutrinos are identical, as assumed in the Standard Model [1]. A measurement of the differential cross section allows, in principle, to determine the Weinberg angle $\sin^2\theta_W$ and to observe the interference which is expected to be destructive for reasonable values of $\sin^2\theta_W$. Practically however $\bar{\nu}_e e^- \rightarrow \bar{\nu}_e e^-$ only has a good sensitivity to both effects, while $\nu_e e^- \rightarrow \nu_e e^-$ essentially probes the interference.

In addition, provided their magnetic moments are nonvanishing, neutrinos will have electromagnetic interactions, making them scatter from a left-handed active state, from the point of view of weak interaction, into a sterile right-handed state.

* Corresponding author. Tel.: +41 32 718 2906; fax: +41 32 718 2901; e-mail: jean-luc.vuilleumier@iph.unine.ch.

[1] Present address: Laboratori Nazionali del Gran Sasso, I-67010 Assergi, Italy.

[2] Present address: CERN, CH-1211 Genève 23, Switzerland.

PII S0168-9002(97)00724-9

The differential cross section for $\bar{\nu}_e e^-$ or $\nu_e e^-$ scattering is given by [1,2]

$$\frac{d\sigma}{dT} = \frac{G_F^2 m_e}{2\pi}\left[(g_V + x + g_A)^2 + (g_V + x - g_A)^2\left(1 - \frac{T}{E_\nu}\right)^2 + (g_A^2 - (g_V + x)^2)\frac{m_e T}{E_\nu^2}\right] + \frac{\pi\alpha^2\mu_\nu^2}{m_e^2}\frac{1 - T/E_\nu}{T} \quad (1)$$

with E_ν the incident neutrino energy, and T the electron recoil energy. Here the first line gives the contribution of the weak interaction to $\nu_e(\bar{\nu}_e)e^- \to \nu_e(\bar{\nu}_e)e^-$ scattering, with

$$g_V = 2\sin^2\theta_W + \frac{1}{2}, \qquad g_A = \begin{cases} \frac{1}{2} & \text{for } \nu_e, \\ -\frac{1}{2} & \text{for } \bar{\nu}_e \end{cases}$$

in the Standard Model; x is calculated from the neutrino form factors, for Dirac neutrinos it is related to the square charge radius $\langle r^2\rangle$ of the neutrino

$$x = \frac{2M_W^2}{3}\langle r^2\rangle \sin^2\theta_W \quad \text{for } \nu_e,\ x \to -x \quad \text{for } \bar{\nu}_e. \quad (2)$$

The second line in Eq. (1) gives the contribution from $\nu_e(\bar{\nu}_e)e^- \to \nu_\ell(\bar{\nu}_\ell)e^-$ ($\ell = e, \mu, \tau \ldots$), with

$$\mu_\nu = \sqrt{\sum_\ell |\mu_{e\ell}|^2},$$

the effective magnetic moment, and $\mu_{\ell\ell'}$ the neutrino magnetic moment matrix [3]. This matrix can either be Dirac like, in which case both static ($\ell = \ell'$) and transition ($\ell \neq \ell'$) moments may be non-zero, or Majorana like, in which case the transition moments only may be finite, the static moments being exactly zero.

1.1. The neutrino magnetic moment

The magnetic moment of the neutrino is an interesting feature. Models exist in which it can become relatively large, while the masses remain reasonably small [4–9]. If large enough, the magnetic moment will affect the cross section for all neutrino interactions, and cause neutrinos to precess in magnetic fields. This may lead to important effects in astrophysical systems.

Such a moment might be responsible for the observed low flux of ν_e from the sun in the ^{37}Cl [10], GALLEX [11], SAGE [12], and Kamiokande [13] experiments. The most popular explanation is resonant neutrino oscillations in the matter of the sun (see Ref. [14]). But, as an alternative, one may invoke a neutrino magnetic moment of order 10^{-10}–$10^{-12}\mu_B$, causing the neutrinos to flip from the left-handed original ν_e flavor eigenstate to a right-handed sterile state in the sun's magnetic field [3,15,16].

Other astrophysical observations suggest that moments of that order would be of the Majorana type. Indeed if neutrinos were Dirac particles, then the observed duration (several seconds) of the SN1987A neutrino burst implies much smaller values: $\mu_{\ell\ell'} < 1$–$20 \times 10^{-13}\mu_B$ [17–19]. These limits assume that right-handed neutrinos are sterile and can escape from the supernova, and in any case do not apply to Majorana neutrinos. Limits from stellar cooling apply to both Dirac and Majorana neutrinos, but are less stringent $\mu_{\ell\ell'} < 10^{-12}$–$10^{-11}\mu_B$ [2,20–23]. This is not in strong conflict with magnetic moments of the strength considered, if one takes into account the model dependence of the astrophysical calculations.

Clearly, it is desirable to obtain unambiguous informations on the neutrino magnetic moment in laboratory experiments, in particular on that of the electron neutrino. The best way to do so is precisely to study in detail $\nu_e(\bar{\nu}_e)e^-$ scattering. The contribution of the weak interaction terms to the total cross-section increases linearly with E_ν. The corresponding contribution from the magnetic moment interaction increases only logarithmically. Experiments with low energy neutrinos are thus best suited.

2. Present experimental situation

Beam dumps at intermediate energy accelerators produce ν_e with energies from 0 to 50 MeV. The fluxes are not very high however, and the ν_e are accompanied by equal numbers of ν_μ and $\bar{\nu}_\mu$, which complicates the interpretation of the experimental data. A measurement of $\nu_e e^- \to \nu_e e^-$ scattering has been performed at the LAMPF beam dump [24]. In spite of a limited statistics the experiment showed that there was no room for a constructive interference, and confirmed the destructive interference. As expected the experiment did not give a precise value for the Weinberg angle. It produced however an upper limit for the magnetic moment of the ν_μ: $\mu_\nu < 1.08 \times 10^{-9}\mu_B$ [25].

Nuclear reactors produce lower-energy neutrinos, and are thus more attractive. They are copious sources of $\bar{\nu}_e$ with energies between 0 and 8 MeV and are ideally suited for such an experiment. The energy spectra are known with good precision, better than 3% for E_ν between 1.5 and 8 MeV [2,26,27]. Fig. 1 shows the expected electron recoil spectrum at a ^{235}U reactor, using Eq. (1) and taking $\sin^2\theta_W = 0.22$. The contribution of the weak interaction is shown, as well as that from a magnetic moment $\mu_\nu = 10^{-10}\mu_B$ alone. One sees that the lower the electron recoil the better the sensitivity to the magnetic moment.

Only few attempts have been made to measure $\bar{\nu}_e e^-$ scattering. The UC Irvine group led by Reines [28] built the first dedicated detector, which was operated successfully at the Savannah River Plant (SRP), observing the process for the first time. The detector consisted of a 15.9 kg plastic scintillator, coarsely segmented and surrounded by a NaI counter, a Pb shield and a liquid scintillator to veto cosmics. The signature for a good event was given by a sin

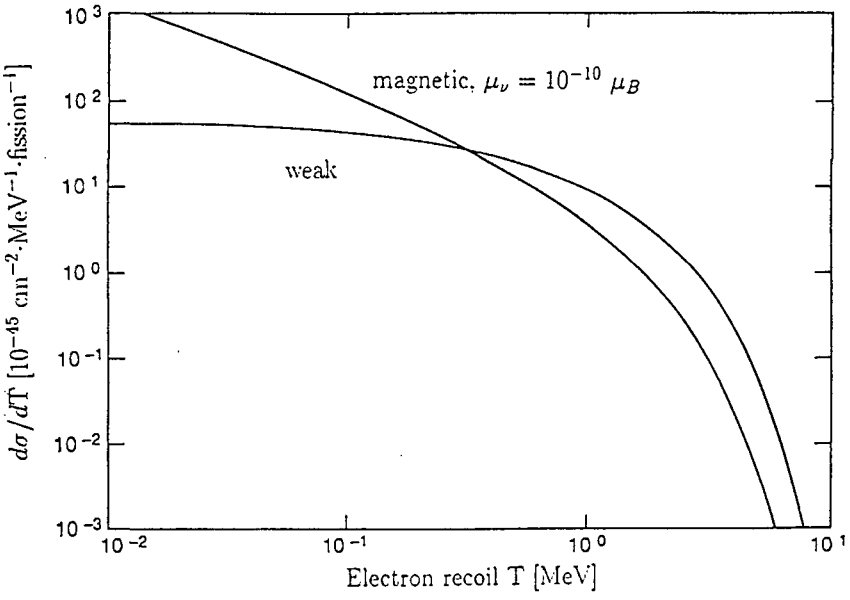

Fig. 1. Expected spectrum of recoil electrons from the reaction $\bar{\nu}_e e^-$ at a ^{235}U reactor. The contributions of the weak interaction alone and of the magnetic term with $\mu_\nu = 10^{-10}\mu_B$ are shown.

Table 1
Event rate in the Savannah River and Kurtchatov experiments

	T (MeV)	Events day^{-1}		
		Reactor on	Reactor off	on–off
Savannah River	1.5–3	45.1±1.0	39.2±0.9	5.9±1.4
	3–4.5	2.4±0.19	1.2±0.14	1.2±0.25
Kurtchatov	>3.15	8.27±0.18	7.49±0.31	0.78±0.36

count in one of the elements of the plastic scintillator with nothing in coincidence. The NaI gave a good anti-Compton efficiency allowing an efficient suppression of the γ background. Events from the $\bar{\nu}_e + p \rightarrow e^+ + n$ reaction in the plastic (200 events day^{-1}!) were efficiently identified by the detection of the annihilation γ rays and/or by the delayed neutron capture signal in the plastic scintillator or in the NaI, and rejected.

The detector was placed at 11.2 m from the core of the reactor operated, at the time, at a power of 1800 MWth, so that the neutrino flux was around $1.9 \times 10^{13}\ cm^{-2}\ s^{-1}$. Events were recorded during 64.6 days reactor on and 60.7 days reactor off. The count rates in two bins of electron recoil energy T are shown in Table 1.

The reactor spectrum was poorly known at the time when the experiment was performed. Vogel and Engel [2], using the presently best determination of the reactor spectrum and fixing $\sin^2\theta_W$ to the presently accepted value, find that the measured rates in the two energy bins given above are 1.35 ± 0.4 and 2.0 ± 0.5 times larger than the expected ones. Taken literally this discrepancy points to a neutrino magnetic moment $\mu_\nu = (2-4) \times 10^{-10}\mu_B$.

More recently, a group from the Kurtchatov Institute in Moscow has also successfully observed $\bar{\nu}_e e^-$ scattering [29]. The detector consists of seven identical cells, filled with a C_6F_6 based liquid scintillator (103 kg in total), serving as active target material. These cells are viewed by two photomultipliers, one on each side, connected by long light guides to suppress the background from the glass. All the materials chosen are radiochemically very clean, to reduce the background from natural ^{40}K, ^{232}Th and ^{238}U activities, and are essentially hydrogen free, so that there is little background from the reaction $\bar{\nu}_e + p \rightarrow e^+ + n$. The detector is surrounded by various shielding layers to reduce the background from local activities. A plastic scintillator, placed on top of the shieldings, suppresses the background from the cosmics. The neutrino flux, at the detector site, is $3.4 \times 10^{12}\ cm^{-2}\ s^{-1}$.

So far, data have been taken for 250 days with reactor on, and 80 days with reactor off. The observed rates, for recoil energies above 3.15 MeV, are 8.27 ± 0.18 day^{-1}, respectively 7.49 ± 0.31 day^{-1}. The difference gives the reactor associated signal: 0.78 ± 0.36 day^{-1}. It is estimated that 0.1 event day^{-1} comes from the background of the reaction $\bar{\nu}_e + p \rightarrow e^+ + n$, the remaining 0.68 ± 0.36 being due to $\bar{\nu}_e e^-$ scattering. This rate is compatible with expectations, obtained with $\sin\theta_W = 0.23$, and leads to the limit $\mu_\nu < 2.4 \times 10^{-10}\mu_B$ for the neutrino magnetic moment. This result is not in conflict with the UC Irvine one. A third experiment is in progress at the Rovno reactor [30]. A 75 kg stack of Si detectors is used. But at present the background is overwhelming, and the experiment rather inconclusive.

It clearly appears important to improve by a large factor on these results, and clarify the situation.

3. The MUNU experiment

To measure with increased precision $\bar{\nu}_e e^-$ scattering at a reactor we are building a tracking device, a gas time projection chamber (TPC), the drift volume of which serves as electron target. We should thus be able to identify well single electrons originating from inside a predefined fiducial volume. Such a good signature should help in keeping the background down. For instance, multi-Compton events and e^+–e^- pairs inside the drift volume, induced by background gammas, will be rejected. Beta and alpha activities from the walls will be identified as such.

Since we have tracking we will measure not only the recoil energy T of the electron, but also, for the first time, its scattering angle φ_e, which is given by

$$\cos\varphi_e = \frac{T(E_\nu + m_e)}{p_e E_\nu} \quad (p_e \text{ is the electron momentum}).$$

This has two advantages. First, it will allow a simultaneous measurement of signal plus background events in the forward direction, and background events only in the backward direction. Background can thus be measured on-line, while the reactor is on. This is particularly important in the case of a non optimal signal to background ratio, since the reactor off periods are in general too short to reach good statistical precision.

Second, knowing the electron recoil energy and the scattering angle, we can reconstruct the incoming neutrino energy E_ν. This additional information will result in improved sensitivity. As noted in Ref. [31], the weak interaction part of the cross section at zero angle for $E_\nu = m_e c^2$ cancels exactly. In that kinematical region, corresponding to $T = (2/3)m_e c^2$, the magnetic moment term only contributes. The sensitivity to that term is thus maximal. Of course, the number of events falling in that region is low, and the angular resolution will be limited because of multiple scattering at low energy. Nevertheless, this will provide a useful cross-check, helping in reducing the systematic uncertainties.

Several measures are taken to further reduce the background. First, the absorption length of gammas is non negligible compared to the dimensions of our detector. For instance the probability of a Compton scatter in the fiducial volume with the outcoming gamma escaping out of it is large. To identify such events the central TPC is surrounded by an anti-Compton detector. The anti-Compton was an essential feature of the SRP detector.

Next, to reduce backgrounds from natural activities, the detector is made from radiochemically pure materials. The detector medium, CF_4 gas, is hydrogen free, so that the background from $\bar{\nu}_e + p \rightarrow e^+ + n$ scattering will be largely suppressed.

To maximize the count rate the detector will be placed very near one of the Bugey reactors [32]. The exact distance from the core to the center of the detector will be 18.0 m. The reactor power is 2800 MWth, corresponding to about 5×10^{20} $\bar{\nu}_e\,s^{-1}$. The lab has a concrete overburden corresponding to 20 m water equivalent, which gives a modest but welcome suppression of the cosmic rays, and cosmogenic activations.

4. The MUNU detector, general description

To summarize the main parts of the detector, shown in Fig. 2, are:

(1) the 1 m^3 CF_4 TPC as central tracking detector,
(2) the surrounding 50 cm thick anti-Compton scintillation detector, which acts as active shielding,
(3) the lead and polyethylene passive shieldings.

4.1. The time projection chamber

The central tracking detector is a 1 m^3 time projection chamber (TPC) conceptually similar to the Xe TPC presently operated in the Gotthard underground lab by the Caltech-Neuchâtel-PSI collaboration [33,34]. It is filled with CF_4 gas. This gas was chosen for its very high density (3.68 g l^{-1} at 1 bar) and relatively low Z, which reduces multiple scattering. The radiation length is $X_0 = 35.9\,g\,cm^{-2}$. Also, the cosmogenic activation of C and F is reasonably low, an important consideration since we have only a very small overburden to protect the detector.

The maximal pressure is 5 bar, corresponding to a total number of target electrons of $N_e = 5.29 \times 10^{27}$. The actual operating pressure will be determined by the threshold energy. At 5 bar, electron tracks are long enough for good identification with realistic spatial resolution down to 500 keV. The pressure must be reduced if lower energy electrons are to be investigated. The drift properties of CF_4 have been studied by various authors (see Ref. [35] for a summary), and in particular by Schmidt and collaborators in Heidelberg [36]. The drift velocity is very high, $\sim 4\,cm\,\mu s^{-1}$ for an electric field of 120 $V\,cm^{-1}\,bar^{-1}$. The lateral drift is small and would amount to 2.5 mm after 1 m at the same field strength. The longitudinal drift would be somewhat less, around 2.2 mm.

All these parameters have been obtained from measurements at 1 bar and over a drift distance of a few cm. We have shown however that electrons can be drifted over larger distances in 5 bar of pure CF_4 with a mini-TPC prototype. The drift distance is 20 cm and the active diameter 10 cm. To achieve good purity, the gas is circulated continuously through an Oxysorb filter to remove oxygen and a cold trap to remove water and possible freon contaminations. A mean drift length of $L_{drift} = 9^{+9}_{-3}$ m at 5 bar and at 120 $V\,cm^{-1}\,bar^{-1}$ was achieved [37]. This is in principle good enough for

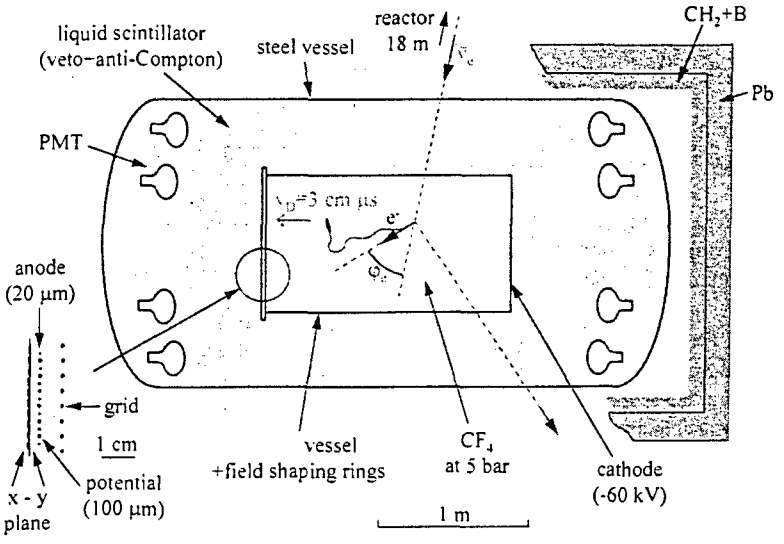

Fig. 2. Layout of the MUNU detector for the study of the $\bar{\nu}_e e^-$ reaction. The central TPC is shown, with the surrounding anti-Compton scintillator, and the various shielding layers. The detector will be installed near one of the Bugey nuclear reactors, at a distance of 18.0 m from the core.

our application. We describe, in Section 7.1, how even larger values have been obtained with the final 160 cm long TPC.

Subsequently, the mini-TPC was modified, and became a scaled down version of the final MUNU TPC [39,40]. It was used to optimize the design of various components. A second version was built, in which the steel vessel was replaced by an acrylic one [41]. It served to verify the possibility of operating a TPC with an acrylic vessel, as well as the compatibility of CF_4 with acrylic.

Measurements of the drift velocity from the pulse length of through-going cosmic muons were also performed with the mini-TPC. The results are in good agreement with previous determinations [35]. In addition spectra obtained with an ^{113}Sn electron conversion source were used to determine the energy resolution. At 5 bar and with a drift field of 120 $V\,cm^{-1}\,bar^{-1}$ it turned out to be better than 20% FWHM at 370 keV.

The 1 m^3 TPC is shown in Fig. 2. The CF_4 gas at pressure up to 5 bar is contained in a cylindrical acrylic vessel of inner diameter 90 cm and 160 cm long. The drift volume is delimited by a cathode on one end of the vessel, and a grid on the other one.

The cathode is held at negative high voltage. Field shaping rings made from copper stripes, 2 mm wide and 0.5 mm thick, are wrapped around the acrylic vessel, with a 1.5 cm spacing. They are tensioned with small springs and interconnected with high voltage 10 MΩ resistors. Still with resistors, the first ring is connected to the cathode and the last one to the grid, in such a way that cathode, shaping rings and grid define an homogeneous drift field inside the acrylic vessel. With this design, the CF_4 volume is active over its entire diameter.

Behind the grid is an anode plane. The inner diameter of the frame is 90 cm. All anode wires are connected together to give the energy signal. The following plane contains two sets of isolated perpendicular strips to pick up the induced signals. The pitch, 3.5 mm, is well adapted to the lateral drift in CF_4. This x–y plane provides the spatial information along the x- and y-axis in the anode plane. The x–y plane is kept at ground potential, while the anode plane is at a positive high voltage large enough to have good amplification around the anode wires. This way the number of high voltage feed-throughs is minimal, which is important for the low background environment. The third coordinate, along the drift field (z) is determined from the time evolution of the signals. This allows a determination relative to the point of the track closest to the grid. The tracks obtained with the mini-TPC, equipped with a similar anode and x–y plane, showed that the spatial resolution is of order $\sigma \simeq 1$ mm in x, y and z direction.

To fully exploit the information provided by the TPC, we have developed a read-out electronics with 8 bit flash ADC's for the anode and each x or y strip. The sampling speed is 40 ns, and the memory size is 1024 words for each channel [42]. The same system will be used for the photomultipliers.

4.2. *The anti-Compton scintillator and the shielding*

The acrylic vessel is immersed in a stainless-steel tank filled with a mineral oil based liquid scintillator provided by Nuclear Entreprises. The attenuation length was measured to be 8 m at 430 nm wavelength. The liquid scintillator serves to veto the cosmic muons and as anti-Compton detector. It is viewed by 48 hemispherical photomultipliers, 24 on each

lid, of 20 cm diameter. The photomultipliers, bought from EMI, are made with low activity glass. They are immersed in the scintillator, along with their bases, and held in place by a polyethylene structure. On the cathode side they are shielded against the electric field generated by the high voltage by a screen made with 100 μm diameter widely spaced tungsten wires.

The photomultipliers will trigger at the one photo-electron level. With this, and considering the scintillator thickness which is 50 cm, the anti-Compton efficiency is about 98% for γ energies above 100 keV.

The liquid scintillator and the steel vessel also serve as low activity shielding. In addition, outside the steel vessel, there are 8 cm of polyethylene to absorb neutrons entering the detector. The first and the last cm are loaded with boron. Still further out are 15 cm of lead, in the form of bricks and pellets held in place by a steel structure, to further reduce gamma activities from outside.

Table 2
Expected $\bar{\nu}_e e^-$ event rates in MUNU

T (MeV)	Acceptance	$\bar{\nu}_e e^-$ Events day^{-1}	
	(Contained)	$\mu_\nu = 0$	$\mu_\nu = 10^{-10}$
0.5–1	0.85	5.3	8.1
>1	0.65	4.2	5.3

Table 3
Background induced by μ^- capture in the CF_4 gas

Interaction	Isotope produced	Events day^{-1}
$\mu^- - {}^{12}C$	^{12}B	3.3×10^{-2}
$\mu^- - {}^{19}F$	^{19}O	6.5×10^{-2}
	^{18}N	4.2×10^{-3}
Total		0.1

5. Event and background rate

The expected $\bar{\nu}_e e^-$ rates at 18 m from the 2800 MWth Bugey reactor have been calculated using Eq. (1), for $\mu_\nu = 0$, taking into account weak interaction only with $\sin^2\theta_W = 0.2325$, and for $\mu_\nu = 10^{-10}\mu_B$, and are given in Table 2. The acceptance for fully contained electrons was estimated by Monte-Carlo simulation using the GEANT code [43].

The total event rate for $T > 0.5$ MeV is 9.5 day^{-1} with no magnetic moment, and 13.4 day^{-1} for $\mu_\nu = 10^{-10}\mu_B$. These rates have to be compared to background rates, which are estimated in the following.

The background rate was calculated assuming a 100 keV threshold for the anti-Compton rejection and a forward angle selection. The threshold in the TPC was set to 500 keV. The simulations were performed with the codes GEANT and GAMTRACK [44]. The main components of the background are due to the cosmics and to natural activities of the materials.

The Bugey lab has a large overburden of steel, concrete and water corresponding to about 20 m water equivalent. Neutrons produced in the atmosphere are practically entirely eliminated, while the muon flux was measured to be 32 m^{-2} s^{-1}. Some μ^-'s stop in the gas and are captured in nuclei, leading to a cosmogenic β activity [45]. But this only contributes a fraction of an event per day (Table 3) to the background rate. Neutrons however are also created in these μ^- captures. These neutrons can then be captured in hydrogen nuclei in the scintillator or in iron and lead nuclei in the shielding, producing gamma rays (Table 4). These γ's in turn produce Compton electrons, which lead to a non negligible background. In all, the background rate of cosmic origin is estimated to be about 2 events per day.

The other important component is that from natural activities. Great care was taken to select radiochemically clean components for the construction of the detector. For the materials entering in large quantity, near the fiducial volume, namely the acrylic for the vessel and the mineral oil for the scintillator, neutron activitation measurements have been performed [46]. The scintillator itself was also tested after the addition of the pseudocumene and the wavelength shifters to the oil. In these measurements sensitivities of order 10^{-13} g g^{-1} to ^{40}K contaminations, and 10^{-12} g g^{-1} to ^{232}Th and ^{238}U contaminations are achieved.

Gamma activity measurements were also made using various low background Ge detectors. The facilities of the Gran Sasso underground laboratory [47] and of the Fréjus underground laboratory [48] were used in specific cases. In addition heavy use was made of our own Ge detectors in the Vue-des-Alpes underground lab and in the laboratoire des basses activités in Grenoble. The sensitivity to ^{232}Th and ^{238}U contaminations is only of order 10^{-10} g g^{-1}, assuming secular equilibrium, but other nuclides such as ^{137}Cs or ^{60}Co can be searched for. All components entering in smaller quantities in the construction of the central TPC and of the anti-Compton detector were selected by gamma spectrometry only. This includes the materials to fabricate the anode, grid and x–y planes, the flat signal cables with their connectors, the components of the resistor chain of the TPC, the field shaping rings, the pseudocumene and the wavelength shifters, the bases of the photomultipliers and the photomultipliers themselves.

Table 5 lists the measured activities of various materials or components used for the MUNU detector. For complex components the numbers quoted are the weighted average values of the activities measured for each subcomponent.

In all the background rate from natural activities, essentially due to Compton electrons induced by the γ activity, is estimated to be about 4 events per day.

Table 4
Major backgrounds induced by neutrons in materials of the MUNU detector

Neutron capture		Events day^{-1}			Events day^{-1}
		Neutron creation site			Total
Medium	Type	Liquid + acrylic	Steel vessel	Shielding	
Gas	$^{19}F(n,x)X^*$	0.038	0.006	0.018	0.06
Liquid + acrylic	$H(n,\gamma)^2H$	0.18	0.25	0.36	0.79
Steel vessel	$^{56}Fe(n,\gamma)^{57}Fe$		0.17	0.42	0.59
Shielding	$H(n,\gamma)^2H$		0.01	0.16	0.17
	Pb, $Fe(n,\gamma)X$			0.07	0.07

Table 5
Measured radioactive contamination of various materials or components used for the construction of the MUNU detector

Medium	Contaminations			
	A	unit g g^{-1}	Meas.	Upper limit
Acrylic	U	10^{-12}		3.00
vessel	Th	10^{-12}		4.00
	K	10^{-7}	2.00	
Steel	U	10^{-9}	0.03	0.87
vessel	Th	10^{-8}	0.18	0.34
	Cs	10^{-18}	0.42	0.93
	Co	10^{-19}	0.76	1.08
	K	10^{-5}	0.14	0.14
P.M.T	U	10^{-7}	0.41	
	Th	10^{-7}	0.49	
	Cs	10^{-18}		2.00
	Co	10^{-19}	0.56	
	K	10^{-4}	0.85	
Liquid	U	10^{-12}		3.00
scint.	Th	10^{-12}		3.00
	Cs	10^{-20}	0.20	
	K	10^{-8}	0.30	

The background generated by $\bar{\nu}_e p \rightarrow e^+ n$ charged current interactions in the acrylic and the liquid scintillator is negligible (Table 6). The total background is thus estimated to be of order of 6 events per day, with a threshold of 500 keV in the TPC.

5.1. Signal versus background, capability of the experiment

The total background rate which will be measured during two reactor-off periods (~2 months) is thus expected to be smaller than the signal rates for $T > 0.5$ MeV (Table 2). We remind that the background will be also determined with better precision from the event rate in the backward half sphere and subtracted. The isotropy of the background could be verified by relaxing some of the selection conditions. Considering the signal rates at 18.0 m in Table 2, a statistical error less than 3% should be achievable in the bin $0.5 < T < 1$ MeV in one year of measuring time. Combined with a systematic error of 5%, essentially from the reactor spectrum (3%), reactor power and burn-up (2%) and

Table 6
Calculated background rate from the reaction $\bar{\nu}_e - p$ in the liquid scintillator and the acrylic

Neutron interaction		Events day^{-1}
Medium	Type	
Gas	$^{19}F(n,\gamma)^{20}F$	2.13×10^{-3}
Liquid + acrylic		
	$H(n,\gamma)^2H$	0.251
Total		0.253

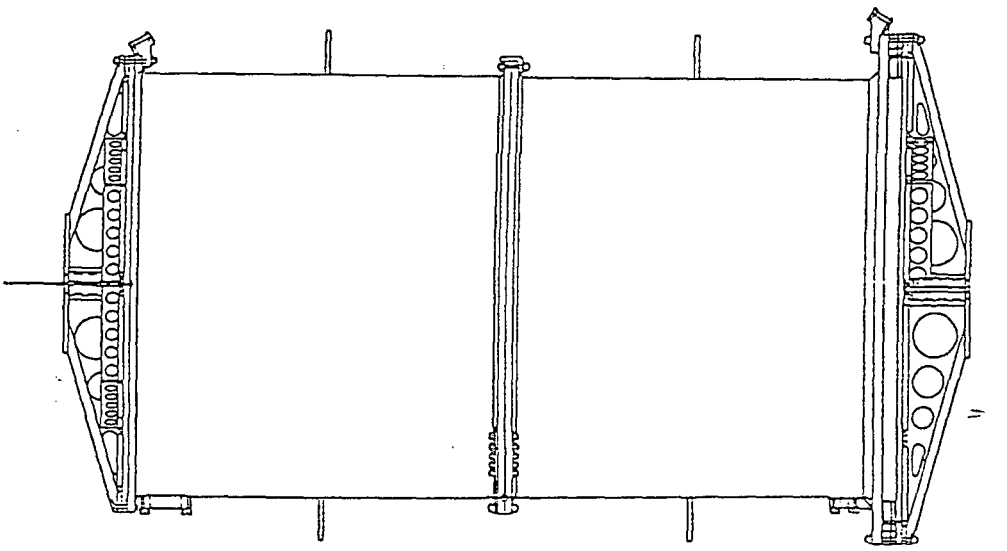

Fig. 3. The acrylic vessel. The cathode side is on the left. The flanges to connect the gas in and gas out pipes are shown at the bottom of the cylinder.

detection efficiency (3%), this leads to a sensitivity to the magnetic moment of the neutrino of

$$\mu_\nu \sim 3 \times 10^{-11} \mu_B,$$

a factor 10 better than in previous experiments. This sensitivity is mainly limited by the systematic uncertainties and changes only slowly as a function of the signal versus background ratio. The limit value on μ_ν would be around $4 \times 10^{-11} \mu_B$ if the background is increased by a factor of 4.

The signal rate for the bin $T > 1$ MeV (4.2 day^{-1}) from weak interaction alone is equivalent to that in the lower energy $0.5 < T < 1$ MeV bin (5.3 day^{-1}), while the contribution from the magnetic moment term is more than a factor of two lower. Using the ratio of the rates in these two energy bins, we will be able to cross check with reduced systematics the contribution of the magnetic moment. This requires however larger statistics, and a significantly longer data taking time. Also, as explained in Section 3, the study of the angular distribution of the recoil electrons will provide a useful cross-check, allowing to reduce systematic uncertainties. Our detector is the first one to measure not only the electron kinetic energy, but also the scattering angle.

Depending on the actual background, the threshold may be lowered, say down to 300–350 keV. To have tracks of reasonable length, it will be necessary to lower the pressure at the same time, say to 3 bar. The event rate should remain essentially unchanged since the electron recoil spectrum peaks at low energy. A sensitivity around $2 \times 10^{-11} \mu_B$ seems then achievable.

We would also like to add that a change of $\pm 5\%$ in $\sin^2 \theta_W$ changes the event rate by 4.3% in the energy bin 0.5–1 MeV, and by 5.8% above 1 MeV. A 5% determination of $\sin^2 \theta_W$ appears thus possible in our experiment, assuming a small magnetic moment. This accuracy is rather good, considering that we are dealing with a purely leptonic process. It is comparable to that achieved by the CHARM II collaboration in the study of ν_μe scattering [49].

6. Detailed description of the MUNU time projection chamber

Having given a general description of the experiment, we now present in more details the central component of the MUNU detector, namely the time projection chamber with its gas handling system. Results of first tests are presented, including a new measurement of the attenuation length in the CF_4 fill gas. These demonstrate the feasibility of the experiment.

6.1. The acrylic vessel

The acrylic vessel is shown in Fig. 3. It is made with as little material as possible to minimize the inactive volume. All the parts are made from acrylic selected for low radioactivity. The vessel is of cylindrical shape, with an inner diameter of 90 cm, and a length of 162 cm, and is closed with two lids. The central cylinder is split up into two pieces small enough to go through the entrance of the laboratory under the reactor. Acrylic glue was used to assemble all the parts of the cylinders and the lids.

The wall thickness of the cylinders is only 0.5 cm. To give more strength, a reinforcing ring has been glued in the middle of each piece, in addition to the flanges at both ends. These are used to bolt the two cylinders together, and the lids to the cylinders. Delrin bolts were chosen. The two lids

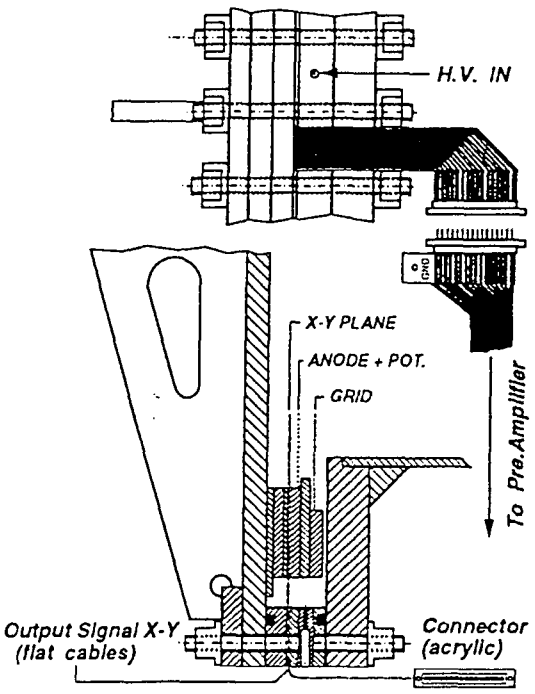

Fig. 4. The frames of the anode and x–y planes on the lid of the acrylic vessel.

are 1.2 cm thick plates reinforced with an octagonal structure. The seals between the two cylinders and between the cylinders and the lids are made with Viton O-rings (Fig. 4). On one side, a spacer ring was squeezed between the lid and the flange, to make room for the frames of the read-out planes (anode and x–y, Section 6.3).

The total weight of the acrylic vessel is ~100 kg. It was tested that the acrylic vessel can stand a pressure difference between inside and outside of up to ±100 mbar, more than the difference in hydrostatic pressure between top and bottom, when in the steel vessel filled with liquid scintillator.

The acrylic vessel is attached to the large steel vessel by acrylic bars. Most are on the top side, arranged radially: three at each end, and five at the center. An additional plate is screwed to the bottom center. These pieces are strong enough to counterbalance the buoyancy. One additional advantage of acrylic for these pieces is that it transmits the scintillation light.

To avoid excessive pollution of the CF_4 gas the vessel must be thoroughly outgassed before filling. Before pumping for the first time the vessel was cleaned with deionized water and then with pure hexane. We then had to pump for a rather long period (~4 weeks) keeping the vessel at a temperature of 60°C in order to reach a residual pressure of 10^{-5} mbar inside the chamber.

To reduce mechanical stress during this initial pumping, the acrylic chamber was placed inside a cylindrical stainless steel vessel similar to the one to be used in Bugey but of smaller size (inner diameter 120 cm). The steel vessel was evacuated at the same time as the acrylic vessel. For convenience reasons all of the early tests of the TPC described in this paper were performed in that configuration.

6.2. Gas handling and purification

An active pressure equalizing system maintains the same pressure, within at most 20 mbar, inside the two vessels, not only while pumping, but also during all subsequent operations: filling with CF_4 gas to a given pressure, measurements at that pressure, gas recuperation.

The active pressure equalizing system measures the pressures in both vessels with electromechanical gauges, as well as the pressure difference with a third gauge. While evacuating it adjusts the pressures by opening and closing electromechanical valves on the steel vessel and acrylic vessel vacuum lines. While filling, it activates valves on the CF_4 line for the acrylic vessel, and a nitrogen line to pressurize the steel vessel. In normal mode, it maintains the pressures constant by activating not only the CF_4 and nitrogen inlet valves, but also valves to release these gases.

A scheme has been devised to recuperate the CF_4 gas before opening the detector for servicing. The bottom part of the gas cylinder for CF_4 storage is immersed in liquid nitrogen, and connected to the acrylic vessel, so that CF_4 starts condensating. During the entire procedure, the gas pressure equalizing system controls the pressure difference between the steel vessel and the acrylic vessel. When the pressure in the acrylic vessel has dropped below 100 mbar, and most of the CF_4 has been recuperated, the cylinder is isolated. Dry nitrogen is introduced into the acrylic vessel before opening, to avoid water adsorption on the walls. This reduces considerably the time required to achieve good vacuum in the acrylic vessel at the next pumping.

The same pressure equalizing system will be used in Bugey to regulate the pressure on the CF_4 gas inside the acrylic vessel and on a nitrogen blanket for the liquid scintillator inside the steel vessel.

The gas introduced into the chamber is the cleanest CF_4 commercially available (99.999% pure). It is circulated continuously through an Oxysorb filter from Messer Griesheim to remove oxygen and water, and through a cold trap to remove possible freon contaminations. The circulation pump is a two metal bellows pump which can work at 7 bar pressure and maintain a flux up to 1500 l/h. The cold trap consists of a steel tube spiral, through which CF_4 is flowing, immersed in an ethanol bath kept at a constant temperature just above the boiling point of CF_4, −95°C, at 5 bar. The cooling power of the trap is 70 W at −95°C.

6.3. The drift field, the anode and x–y planes

The cathode, a plain 0.2 mm thick copper plate, is screwed to one of the lids of the acrylic vessel. The frames for the x–y plane, anode plane and grid are screwed to the other lid. The cathode, grid and field shaping rings define a

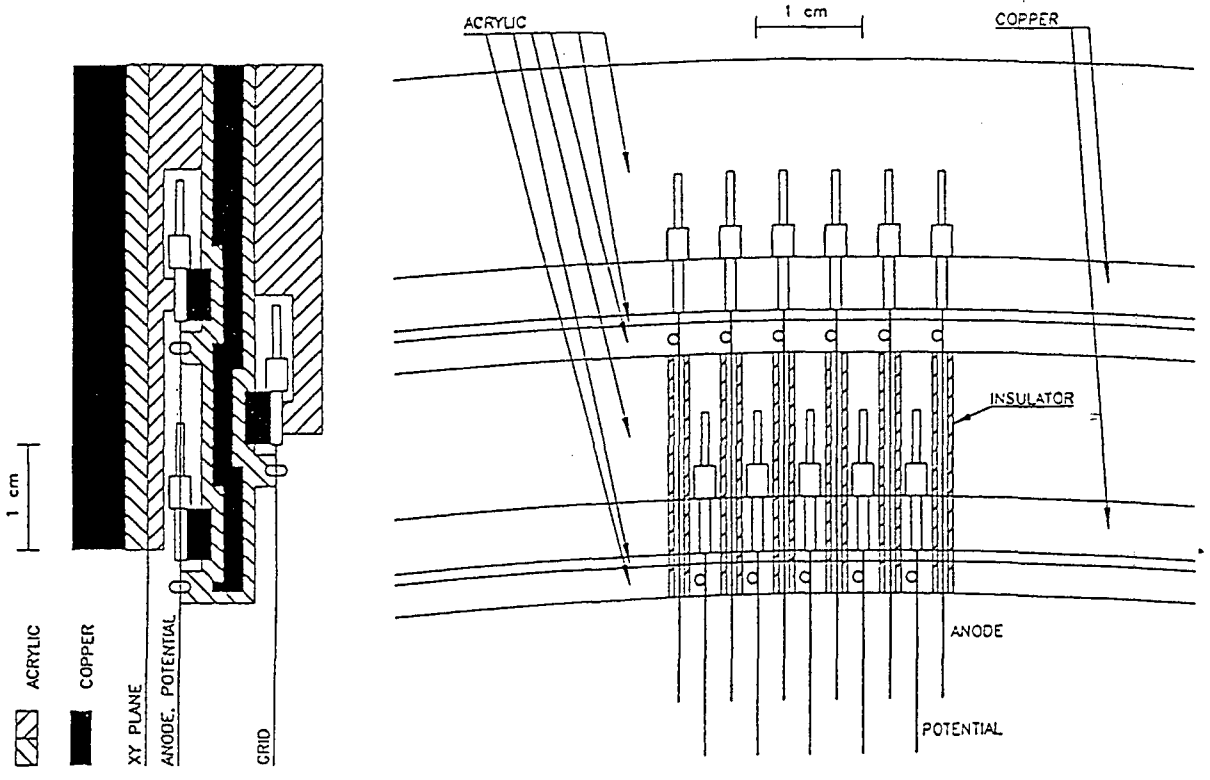

Fig. 5. The frame of the wire planes for the MUNU TPC.

homogeneous electric drift field in the entire volume of the vessel. The cathode is maintained at a negative high voltage of up to −80 kV. The connection is made at the center, with a cable traversing axially the steel vessel. The grid is held at a negative potential, as described later. Cathode and grid are connected with a resistor chain on the outside of the acrylic vessel. After each resistor (10 MΩ), contact is made with a field shaping ring. The spacing is 15 mm. The rings themselves are made from phosphorous bronze wires (∅ 0.7 mm, 94% copper and tin) and tensioned with springs made from the same material around the acrylic vessel.

The anode and grid planes are mounted on both sides of one single ring, of 90 cm inner diameter, matching the active diameter of the chamber (see Fig. 5). The core is a copper ring, providing the mechanical stiffness. For electrical insulation it is sandwiched between two acrylic rings glued one on the grid side, the other one on the anode side.

The anode plane contains the anode wires themselves, with a spacing of 4.95 mm, alternating with potential wires for electrical separation. The anode wires (∅ 20 μm) and the potential wires (∅ 100 μm) are made from pure tungsten. The anode wires are mounted on a narrow copper ring, itself glued on the acrylic ring. The potential wires are attached to a second copper ring, identical to the first one, except for the smaller diameter. The wires are crimped in small hollow copper needles, of inner diameter 200 μm, held in place in grooves machined in the copper rings. For long-term stability the anode wires are glued to the needles at the rear end by a droplet of acrylic glue. The mechanical tension is 60 g for the anode wires, just beyond the limit of elasticity, and 200 g for the potential wires. The electrical contact between the anode wires, or the potential wires, is provided by the copper rings.

The lateral position of the wires is defined to within 10 μm by small pins against which they are pushing. The anode wires are isolated from the potential wires by U-shaped Delrin insulators on the frame, and over a distance of roughly 1 cm beyond it.

The grid wires are also made from plain tungsten and have a diameter of 100 μm. They are mounted in a similar way, the grid wires being perpendicular to the anode wires. The distance between the grid and anode planes is 8.5 mm. The design chosen ensures good mechanical precision, in particular for the anode and potential wires, which is important for the uniformity of the gain.

The x–y plane is a 125 μm thick mylar foil covered on both sides with a 35 μm copper film. The strips, x on one side and y on the opposite one, are made by etching. The strips are diagonal with respect to the anode and grid wires. To have a uniform lattice the spacing between strips is 3.5 mm, which is that between anode wires, 4.95 mm, divided by $\sqrt{2}$. The pattern (Fig. 6) is such that the screening between

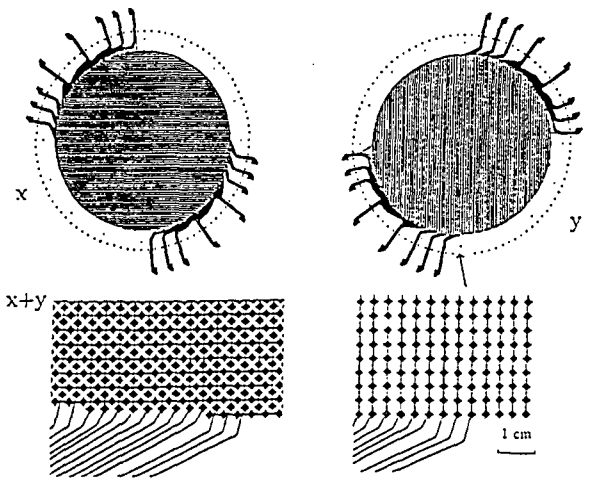

Fig. 6. Schematics of the x–y plane.

x and y strips is minimal. The foil is stretched and glued on a 1 mm thick acrylic ring, for electrical insulation, itself glued on a copper ring, for stiffness. This frame is screwed, along with the frame for the anode and grid planes on the lid of the acrylic vessel (Fig. 4). The x–y plane is located 3 mm behind the anode plane (Fig. 5).

In total, there are 512 strips, 256 x and 256 y. At the edge, the mylar foil extends into 32 flat cables. The strips are brought together, in groups of 16, which are led into the 32 flat cables. The flat cables leave the lid of the acrylic vessel through slots in the edge of the spacer ring. These slots are sealed with acrylic glue. These cables are crimped to home-made low activity connectors outside the vessel, connected in turn to 2 m long flat cables made in a similar way. These long cables are, however, covered with a thin insulating layer. They carry 16 signal leads on one side and a ground strip on the other one. They are bundled in 4 groups of 8 which go to 4 feed-throughs in the steel vessel, through a labyrinth in the shielding, to preamplifiers located outside the Pb shielding (Fig. 7). This arrangement minimizes the absorption of scintillation light by the cables. Also the detector is shielded against radio-activities from the preamplifiers. To minimize the electronic noise, it was necessary to shield electrically the cables along the portion outside the steel vessel with great care.

To avoid soldering all electrical connections are made with connectors, crimps, or screws. Solder is a problem from the point of view of radiopurity, as it contains ^{210}Pb. All the glueing was done with acrylic glue, which was found to be sufficiently clean.

In normal operation the x and y strips are maintained at ground potential at the input of the preamplifiers. The anode wires are maintained at a positive potential sufficient for reasonable amplification. The potential wires are held at ground potential, or at a positive potential significantly lower than that of the anode. Since the distance from the grid to the anode is larger than that from the anode to the

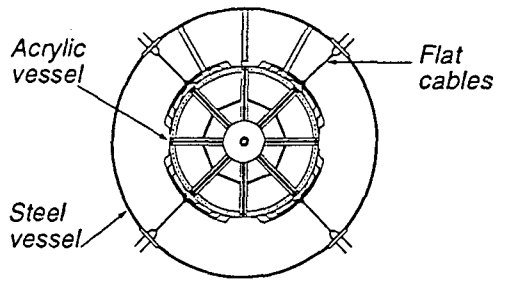

Fig. 7. Arrangement of the flat cables for the x and y strips. The steel vessel and the acrylic vessel are shown.

x–y plane the grid wires are held at a negative potential. Specific potential configurations are given in Section 7.2.

Each x and y strip has its own preamplifier, operated in current–voltage mode (270 mV μA^{-1}). The design is based around a LeCroy TRA1000 circuit. The rise time of the signals at the output of the preamplifier is around 200 ns. In normal operation, the preamplifier signals are sampled every 40 ns with 8 bit FADC's (Struck DL350 system). The input range extends from 0 to −600 mV. The response function is non-linear to increase the amplitude resolution for small signals. A 1024 word memory is associated to each channel. The anode wires, coupled together by the copper ring, are connected to a single similar preamplifier, sampled in the same way. This additional information makes it often easier to identify ends of tracks from the increased dE/dx, and to single out α particles. event is best determined by integrating the anode signal.

7. Test measurements

7.1. Anode signals and attenuation length measurements

In a first series of tests we verified that our gas handling system works satisfactorily. For these, as mentioned earlier, the acrylic vessel was mounted in a steel vessel similar to that to be used in Bugey, but of smaller size. The acrylic vessel was resting horizontally on spacers on the bottom of the steel vessel. The connections to the gas circulation system and to the pressure equalization system were the same as in the final design. The steel vessel was not filled with liquid scintillator, however, but with nitrogen, at the pressure determined by the gas pressure equalization system, slightly below that in the acrylic vessel.

The acrylic vessel was equipped with the cathode, the field shaping rings, the grid and the anode. Only 16 x and 16 y strips were connected to flat cables and brought out of the steel vessel. The other ones were grounded outside the acrylic vessel.

We looked at anode signals induced by cosmic muons to verify that the gas purification system brings the gas to a level of purity sufficient to drift electrons. Measurements

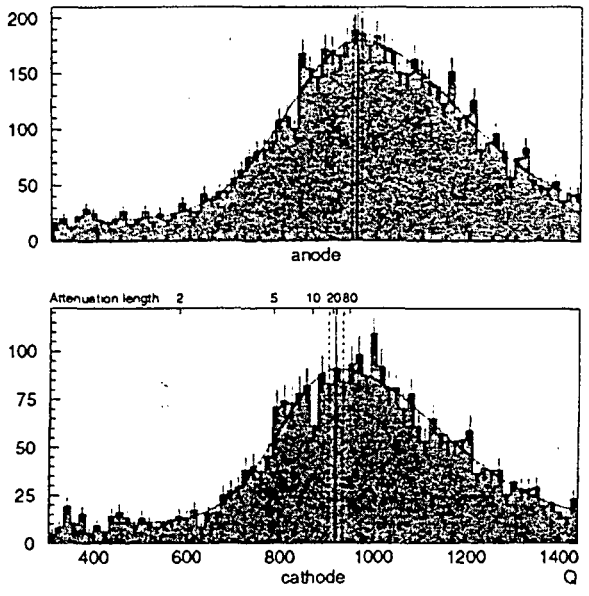

Fig. 8. Measured energy deposition of nearly vertical cosmic muons crossing the TPC at 30 cm from the anode (top) and 30 cm from the cathode (bottom), at 3 bar and with a drift field of 50 V cm^{-1} bar^{-1}. The fitted peak position is indicated. The upper horizontal axis of the bottom spectrum shows the attenuation length for a given peak position.

were performed at 1 and 3 bar, with a drift field ranging from 50 to 80 V cm^{-1} bar^{-1}. At the latter field strength the drift velocity was 3.2 cm μs^{-1} bar^{-1}.

Two plastic scintillators covering an area of 40 × 40 cm^2 were placed one on top of the steel vessel, the other one just below. They were used as a telescope to tag muons entering nearly vertically into the detector. Data were taken with the telescope axis at a distance of 30 cm from the anode, and 30 cm from the cathode. Signals induced by these muons are relatively short since the tracks are nearly perpendicular to the drift field. After the preamplifier, they were shaped in a spectroscopy amplifier (integration and differentiation constants 5 μs), and analyzed in a multi-channel analyzer. They correspond to an energy deposition of 480 keV at 1 bar, and 1.5 MeV at 3 bar. They give rise to the peaks shown in Fig. 8.

One sees that the peaks for the two telescope settings are essentially in the same position. The fitted peak positions with their uncertainties are indicated. Taking into account that the difference in the drift distances is 1 m, one concludes that the mean atenuation length is

$$L_{\text{drift}} = 22^{+14}_{-6}\ \text{m} \quad \text{at 3 bar}$$

with a drift field of 50 V cm^{-1} bar^{-1}. This is largely sufficient for MUNU.

7.2. The x–y signals

The current in the induced x–y signals is roughly 5 times lower than in the anode signals. The anode high voltage must be adjusted so that they exceed, comfortably, the noise level. Using the connected strips we looked at the x and y signals induced by minimum ionizing nearly vertical cosmic muons tagged by the telescope. For these measurements the telescope was placed in the middle of the TPC, at equal distance from the anode and the cathode.

Reasonably large signals, namely of order 5–10 mV, were observed with a digital oscilloscope at anode and grid voltages of +1850 V, respectively, −3330 V at 1 bar, and +2570 V, respectively, −4625 V at 3 bar, the potential wires being maintained at ground potential. The drift field was 60 V cm^{-1} bar^{-1}. This signal amplitude is adequate, since the rms noise is less than 2 mV. Examples are shown in Fig. 9. These output voltages correspond to an input current of around 70 000 e$^-$/300 ns for the signal, and 14 000 e$^-$ for the noise.

Next the signals were analyzed with the final read-out system, the preamplifiers feeding the DL350 FADC's. In these measurements, performed at 3 bar, the anode and grid voltages were raised to +2700 V, respectively, −4860 V. The x–y plane was oriented so that the x strips were almost vertical, thus measuring the horizontal coordinate. As a consequence, the ionization density is high along the x strips, and close to the minimum on the y strips. This is clearly visible in the example shown in Fig. 10, the measured charge density is higher in the x–z projection of the track than in the y–z projection. But good signal to noise ratio is achieved even for the most unfavorable projection.

To estimate the local spatial resolution, we fitted a straight line through the y–z projection. We then evaluated the average mean squared deviation of the fitted signal centroid on each strip to the line. The square root gives the standard deviation

$$\sigma = 1.6\ \text{mm}$$

which can be considered a measure of the spatial resolution at 3 bar. More elaborate algorithms, which we are developing, will be necessary to fully exploit the spatial resolution when reconstructing tracks of low energy electrons, which curl more than those from through going cosmic muons.

7.3. Energy resolution

Measurements were also made of the energy resolution with an ^{241}Am source emitting 59.5 keV γ-rays. For convenience reasons these measurements were carried out with the actual anode and x–y planes in a shorter steel vessel. The drift volume was defined by a cage supporting field shaping rings and a cathode, the depth of the drift volume being 13 cm. The source was placed outside the steel vessel, on the side of the drift volume. Measurements were made at 3 and 5 bar.

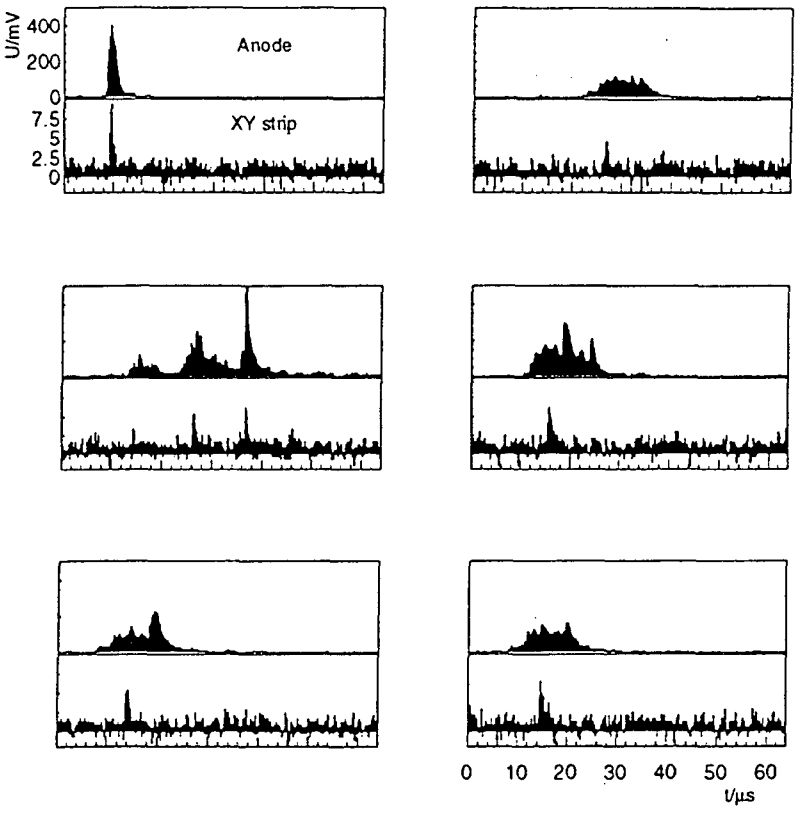

Fig. 9. Examples of signals on the anode and an x strip, measuring the horizontal coordinate, induced by nearly vertical cosmic muons, seen at the output of the preamplifiers.

In these measurements a field configuration calculated with the GARFIELD code [50] was used, the ratio of anode to grid voltage being -1.75. This symmetrizes the electric field with respect to the anode plane, and thus reduces the mechanical stress on the anode wires. As a consequence the sagitta of the anode wires is minimal, and the gain uniformity is improved. The actual anode voltages were 3350 and 4450 V at 3, respectively, 5 bar. The voltage on the potential wires was raised to 400, respectively, 500 V, to avoid discharges between the anode and potential wires. The anode signals were processed as described in Section 7.1. Since the signals are short, the integration and differentiation constants of the shaping spectroscopy amplifier were set to 1, respectively, 1.5 μs. The spectra obtained at 3 and 5 bar of CF_4 are shown in Fig. 11.

The full absorption peak is clearly visible. Fitting a Gaussian to the peaks yields an energy resolution (FWHM) of 28 keV corresponding to 48% FWHM at 3 bar. At 5 bar it is 34 keV, equivalent to 58%. The contribution of the electronics noise is of order 6 keV and is thus negligible. The energy resolution was found to change only little in additional measurements performed at different anode voltages.

Assuming that the energy resolution scales with the inverse square root of the energy, as it does in the Xe TPC operated in the Gotthard lab [34], we expect a resolution of order 20% FWHM at 500 keV. This is in rough agreement with what was observed in that energy range with the mini-TPC (Section 4.1), and is adequate for the MUNU experiment.

8. Conclusion

We have presented MUNU, a new detector for the detailed study of $\bar{\nu}_e e^-$ scattering at a nuclear reactor. The central component is a 1 m^3 time projection filled with CF_4 gas at pressures up to 5 bar. It is surrounded by an anti-Compton scintillator to reduce the background. Radiochemically clean components have been selected for all components. The detector is presently being set up near the Bugey reactor.

First results obtained with the time projection chamber have been presented. A mean attenuation length of $L_{\text{drift}} = 22^{+14}_{-6}$ m at 3 bar with a drift field of 50 V cm^{-1} bar^{-1} was achieved. Under the same conditions the spatial

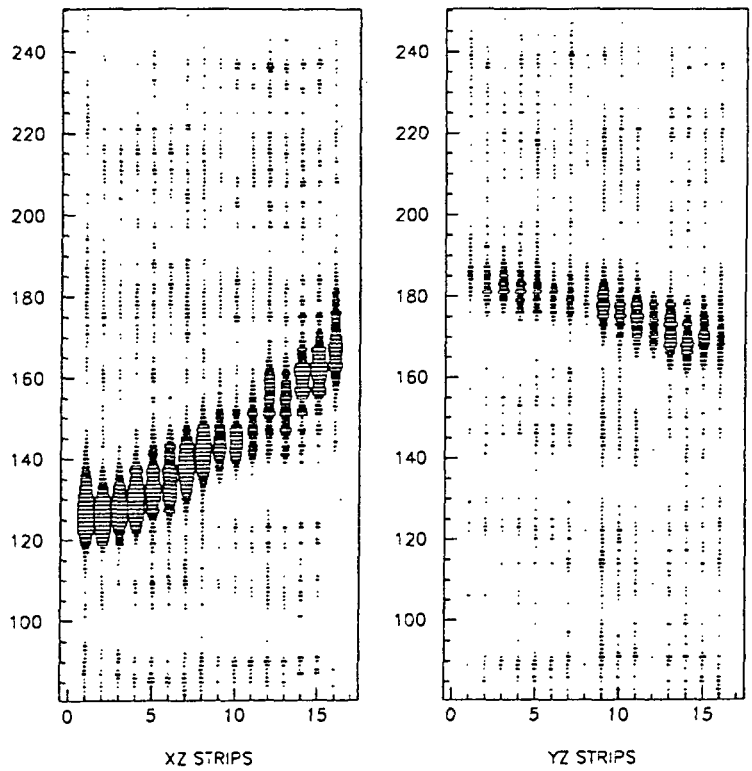

Fig. 10. Cosmic muon tracks (xz and yz projections) observed with the central 16×16 central x and y strips at 3 bar. The distance between two strips (horizontal axis) is 3.5 mm. The vertical z axis is such that 20 channels correspond to 2.56 cm. The area of the rectangles is proportional to the current measured on a strip. Only part of the track is in the overlap region of the x and y strips, so that both projections are displaced along the z-axis.

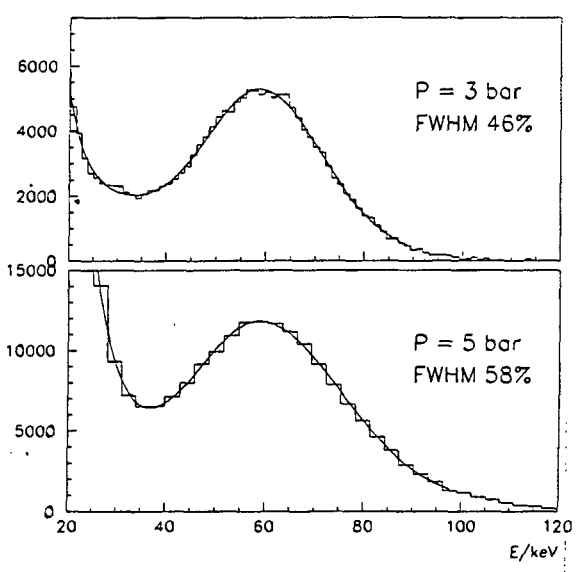

Fig. 11. Energy spectra obtained with the actual anode and x–y plane in the short-time projection chamber (see text) exposed to an ^{241}Am source, at 3 and 5 bar CF_4. The anode voltages were 3350 and 4450 V at 3, respectively, 5 bar.

resolution was determined to be $\sigma = 1.6$ mm. This is largely sufficient for MUNU.

Beyond demonstrating the feasibility of the MUNU experiment, these results show that it is possible to build much larger TPC's for applications in low energy neutrino physics. In particular, a device with a total CF_4 mass of 2 to 8 tons, to be distributed for instance in 4 identical modules, can be contemplated. Such a device, operated at a pressure of 1 to 2 bar, and having a threshold around 100 keV, would be ideally suited to study p–p, ^{7}Be and pep neutrinos from the sun. With the given mass range, the event rate would be between 5 to 20 per day. Since not only the electron recoil energy can be measured, but also the scattering angle, the energy of the incident neutrino can be reconstructed. It would thus be possible to perform solar neutrino spectroscopy. That would lead to a major advance in our understanding of solar neutrinos.

Acknowledgements

The authors are grateful to Herb Henrikson, who designed the acrylic vessel. They thank P. Vogel and J. Bernabeu for enlightening discussions and G. Bovo for his contribution

to the construction of the pressure equalizing system. This work was supported by INFN, IN2P3 and the Swiss NSF.

References

[1] B. Kayser et al., Phys. Rev. D 20 (1979) 87.
[2] P. Vogel, J. Engel, Phys. Rev. D 39 (1989) 3378.
[3] M.B. Voloshin, M.I. Vysotskii, L.B. Okun, Sov. Phys. JETP 64 (1986) 446.
[4] M.B. Voloshin, Sov. J. Nucl. Phys. 48 (1988) 804.
[5] K.S. Babu, R.N. Mohapatra, Phys. Rev. Lett. 63 (1989) 228.
[6] M. Leurer et al., Phys. Lett. B 237 (1990) 81.
[7] R. Barbieri et al., Phys. Lett. B 252 (1990) 251.
[8] S.M. Barr, E.M. Friere, A. Zee, Phys. Rev. Lett. 65 (1990) 2626.
[9] B.K. Pal, Phys. Rev. D 44 (1991) 2261.
[10] B.T. Cleveland et al., Nucl. Phys. B (Proc. Suppl.) 38 (1995) 47.
[11] GALLEX collaboration (P. Anselmann et al.), Nucl. Phys. B (Proc. Suppl.) 38 (1995) 68.
[12] J.N. Abdurashitov et al., Nucl. Phys. B (Proc. Suppl.) 38 (1995) 60.
[13] T. Suzuki et al., Nucl. Phys. B (Proc. Suppl.) 38 (1995) 54.
[14] P.I. Krastev, S.T. Petcov, Phys. Lett. B 299 (1993) 94.
[15] E.Kh. Akhmedov et al., A. Lanza, S.T. Petcov, Phys. Lett. B 348 (1995) 124.
[16] J. Pulido, Z. Tao, Phys. Rev. D 51 (1995) 2428.
[17] J.M. Lattimer, J. Cooperstein, Phys. Rev. Lett. 61 (1988) 23.
[18] R. Barbieri, R.N. Mohapatra, Phys. Rev. Lett. 61 (1988) 27.
[19] D. Notzold, Phys. Rev. D 38 (1988) 1658.
[20] J. Bernstein et al., Phys. Rev. 132 (1963) 1227.
[21] P. Sutherland et al., Phys. Rev. D 13 (1976) 2700.
[22] G. Raffelt, Phys. Rev. Lett. 64 (1990) 2856.
[23] V. Castellani, S. Degl'Innocenti, The Astr. Phys. J. 402 (1993) 574.
[24] R.C. Allen et al., Phys. Rev. Lett. 55 (1985) 2401; Phys. Rev. D 47 (1993) 11.
[25] D.A. Krakauer et al., Phys. Lett. B 252 (1990) 177.
[26] B. Achkar et al., Phys. Lett. B 374 (1996) 243.
[27] G. Zacek et al., Phys. Rev. D 34 (1986) 2621.
[28] F. Reines, H.S. Gurr, H.W. Sobel, Phys. Rev. Lett. 37 (1976) 315.
[29] I.I. Gurevitch et al., preprint, I.V. Kurtchatov Institute of Atomic Energy, 123182. Moscow, Russia, 1991; G.S. Vidyakin et al., JETP Lett. 49 (1989) 740.
[30] A.I. Derbin et al., JETP Lett. 57 (1993) 768.
[31] J. Segura et al., Phys. Rev. D 49 (1994) 1633.
[32] B. Achkar et al., Nucl. Phys. B 434 (1995) 503.
[33] H. Wong et al., Phys. Rev. Lett. 67 (1991) 1218.
[34] J.-C. Vuilleumier et al., Phys. Rev. D 48 (1993) 1009.
[35] A. Peisert, F. Sauli, CERN Yellow Report 84-08, 1984; L.G. Christophorou et al., Nucl. Instr. and Meth. 163 (1979) 141.
[36] B. Schmidt, S. Polenz, Nucl. Instr. and Meth. A 273 (1988) 488; K. Martens, Diplomarbeit, Universität Heidelberg, 1989.
[37] C. Broggini et al., Nucl. Instr. and Meth. A 311 (1992) 319.
[38] MUNU collaboration, The MUNU time projection chamber, Nucl. Instr. and Meth. A, submitted.
[39] V. Joergens, Ph.D. thesis, Institut de physique de l'université de Neuchâtel, 1994.
[40] J. Farine, Ph.D. thesis, Institut de physique de l'université de Neuchâtel, 1996.
[41] C. Broggini, Nucl. Instr. and Meth. A 432 (1993) 413.
[42] P. Giarritta, Diplomarbeit, University of Zurich, 1994.
[43] R. Brun et al., GEANT–CERN Program Library.
[44] G. Bagieu, GAMTRACK, ISN–Grenoble Int. Rep. 1992.
[45] N.C. Mukhopadhyay, Phys. Rep. C 30 (1977) 1.
[46] E. Orvini, University of Pavia, private communication.
[47] C. Arpesella, Nucl. Phys. B (proc. suppl) 28A (1992) 420.
[48] Ph. Hubert, University of Bordeaux, private communication.
[49] D. Geiregat et al., Phys. Lett. B 259 (1991) 499.
[50] R. Veenhof, GARFIELD, CERN program library.